Mercury Amalgam Electrodeposition on Metal Microelectrodes

A Thesis
Presented to
The Academic Faculty

by

Audric Saillard

In Partial Fulfillment
of the Requirements for the Degree
Master of Science in Mechanical Engineering

Georgia Institute of Technology
August 2005

Mercury Amalgam Electrodeposition on Metal Microelectrodes

Approved by:

Dr. Andrei Fedorov, Advisor
School of Mechanical Engineering
Georgia Institute of Technology

Dr. Cyrus Aidun
School of Mechanical Engineering
Georgia Institute of Technology

Dr. Lawrence Bottomley
School of Chemistry & Biochemistry
Georgia Institute of Technology

July 15, 2005

ACKNOWLEDGEMENTS

This year has been an amazing cultural and educational experience for me. I want to first thank my advisor, Professor Andrei Fedorov, and the National Science Foundation, for offering me this opportunity and introducing me to the field of research. Pr. Fedorov trusted me on a project for which I had no specific background, and supported me all year. I am also very grateful to Dr. Peter Kottke, who carefully followed my work and spent a lot of time assisting me on specific problems. Together they taught me the fundamentals of research, as well as the scientific material I needed, with exceptional patience and passion. Finally, I want to thank both of them for understanding my language limitations, the time they spent correcting it, and their great sense of humor, which made my research agreeable.

I am also grateful to Douglas Rudolph, Ph.D. student, and Drs. Christine Kranz, from the School of Chemistry and Biochemistry at Georgia Tech, for sharing with me their precious insight on plating experiments. Particularly, I thank Douglas Rudolph for providing me with specific experimental data, and for its patient answers to my related interrogations. In the same department, I am grateful to my friend and roommate, Justyna Wiedemair, for enriching talks about electrochemistry. I also want to thank my thesis committee members, Pr. Cyrus Aidun and Pr. Lawrence Bottomley, for their attention and advice.

I am grateful to my family for its continuous encouragement, and most particularly my parents and my aunt, Odette Boigey, who provided me with essential financial supports. Finally, I want to thank my friends and especially my girlfriend, Christine Steil, for helping have a great time this year.

TABLE OF CONTENTS

LIST OF FIGURES

LIST OF SYMBOLS

When not specifically defined, the symbols correspond to the following:

Symbol	*Description*	*Unit/Value*
A	area (of the electrode or a subpart)	m^2
D_0	diffusion coefficient	m^2/s
E	Electrode potential (against reference)	V
F	Faraday constant	9.65×10^4 C
N_a	Avogadro number	6.02×10^{23} mol^{-1}
R	molar gas constant	8.31 J mol^{-1} K^{-1}
T	temperature	K
V	volume (of the amalgam or a droplet)	m^3
a	radius of the metal inlaid disk	m
c^b	bulk concentration of the mercury ions	$M = mol/dm^3$
e	*electron charge*	1.60×10^{-19} C
g	gravity constant	9.81 m/s^2
k	*Boltzmann constant*	1.38×10^{-23} J/K
k_m	mean curvature (=2/R for a sphere)	m
m	reduction reaction coeff., defined by eq. (2.1)	-
n	reduction reaction coeff., defined by eq. (2.1)	2
t	time	s
z	ion's charge number	-
δx	length scale	m
λ_D	Debye length	m
τ	time scale	s

Mercury properties

M	Atomic mass	200.59 10^{-3}	kg mol^{-1}
ρ	Density	13.6 10^3	kg m^{-3} at 20°C
μ	Viscosity	1.6 10^{-3}	Pa s
σ	Surface tension	465 10^{-3}	N m^{-1}

SUMMARY

Mercury amalgam microelectrodes, typically fabricated by electrodeposition of mercury onto metal (platinum, gold, silver) inlaid disks, possess certain advantageous properties for scanning electrochemical microscopy (SECM) and electroanalysis. But as applications require more and more precision, fundamental questions concerning the exact shape and constitution of the amalgam can become important for interpreting SECM experimental data. The purpose of this study is to analyze in depth the formation of the amalgam, in order to provide a better understanding of the key physical processes, and so be able to judge of the accuracy of the currently used models and refine them when necessary.

The amalgam formation is the result of several processes that occur roughly at two different scales: the "global" scale, which is microscopic, and the "local" scale, of the order of few nanometers. On the global scale, the dominant physical process is the mass transport, driven almost entirely by diffusion, which determines the rate of mercury deposition. Other phenomena occur at the smaller local scale. Their understanding is essential to predict precisely the volume and shape of the amalgam at shorter times. Among these local phenomena, nucleation and droplet interactions appear critical. The former sets the formation rate and the size of the isolated mercury droplets that are initially formed at the surface of the electrode. An understanding of the latter is necessary to determine the droplet coalescence process.

Among the specific accomplishments of this Master thesis work, a time scale analysis of the "global" phenomena has been performed leading to the conclusion that quasi-steady state diffusion of mercury ions in the bulk mainly defines the electrodeposition rate. Then, a series of analytical formulations for diffusion-limited electrodeposition current available in the literature

has been quickly analyzed, leading to development of analytical/numerical models. These latter have been implemented, and results were critically compared with experimental data, leading to the conclusion that the early electrodeposition was not enough finely modeled. Mercury droplets nucleation and surface interaction have been identified as relevant processes of this period. They have next been investigated in detail, leading to the characterization of the nucleation process, and the derivation of two complimentary approaches on charged droplet stability. “Regime” maps have been developed, providing first explanations and quantitative information on charged droplet stability dependence on potential applied, electrolyte and droplet size. Finally, through analysis of theoretical predictions, a series of electroanalytical experiments have been proposed for the future validation of the suggested theoretical models.

CHAPTER 1

INTRODUCTION

Mercury amalgam microelectrodes has recently become a subject of renewal attention due to their use in scanning electrochemical microscopy (SECM) [1, 2]. SECM technique allows one to characterize chemical and topographical features of the surface of a substrate [3] by moving a microscopic electrode over the interface. This is only possible with microelectrodes, whose small size allows them to reach quickly a steady-state behavior [4]. An electrical potential applied at the SECM working electrode induces an electrochemical redox reaction, that results in a Faradaic current proportional to the net flux of reduced/oxidized species to the electrode surface in the case of transport-limited process. The SECM has also been recently used to study biochemical processes, allowing one to spatially measure surface kinetics and product release [5-7].

Mercury microelectrodes are fabricated by electrodeposition of mercury onto a metal inlaid microdisk. The commonly used substrate metals, platinum, gold or silver, are known to form an amalgam, i.e. an alloy or intermetallic compounds with mercury [8-11]. This kind of electrode presents one significant advantage for SECM: mercury has a high overpotential for hydrogen evolution [12], allowing one to study electrochemical processes occurring in the negative potential range in aqueous solutions, without prompting hydrogen ion reduction. In other words, although thermodynamics would predict reduction of hydrogen ions and formation of hydrogen gas at a potential of zero volts (vs. SHE) regardless of electrode material, the

reaction is kinetically limited on mercury, and the reaction rate is negligible for potentials down to nearly -1 V (vs. SHE) [12].

A critical feature of SECM is the possibility to predict the tip electrode current from the first principles using theoretical models describing the relevant reaction and transport processes. But as the applications demand more and more precision, fundamental questions concerning the exact shape and chemical/phase composition of the amalgam-electrode can become important to the interpretation of the experimental data. Thus, a deeper understanding of the chemical/physical processes involved in the amalgam formation is needed, combined with the development of relevant phenomenological models.

This thesis concerns with the study of electrodepositon of mercury onto a disk microelectrode, mainly focusing on the structural evolution of the deposited phase during the process. Metallurgical aspects of amalgam formation add an additional level of complexity and are beyond the scope of this work. Up to date, most models described in literature consider the mercury electrodeposition as a simple diffusion-limited process associated with a quasi steady-state "penned configuration" amalgam growth [8, 13, 14], "penned configuration" denoting a total coverage of the electrode disk by one mercury volume. In these models, mercury ions are transported via Fickian diffusion to the surface of the electrode, where they are absorbed and reduced in an infinitely fast process to produce the liquid mercury phase, increasing its volume as the time progress. The growth and the morphology evolution of the mercury deposit are assumed much faster than the mass transfer, so the shape of the liquid mercury phase is assumed to proceed through equilibrium states. Therefore, the shape of the amalgam is determined by an energetically favorable state, requiring a minimum interface area. This modeling predicts a

smooth and regular evolution of the plating current, which does not constitute a reliable description of the experimental plating curves, as illustrated in Figure I-1.

In this study, our objective is to carefully check the validity of these common made assumptions and simplifications, and then identify, investigate and model the processes so far neglected but apparently relevant. Development of such an improved understanding and modeling capability is a first step towards design of an optimal procedure for making SECM mercury electrodes of a controlled shape.

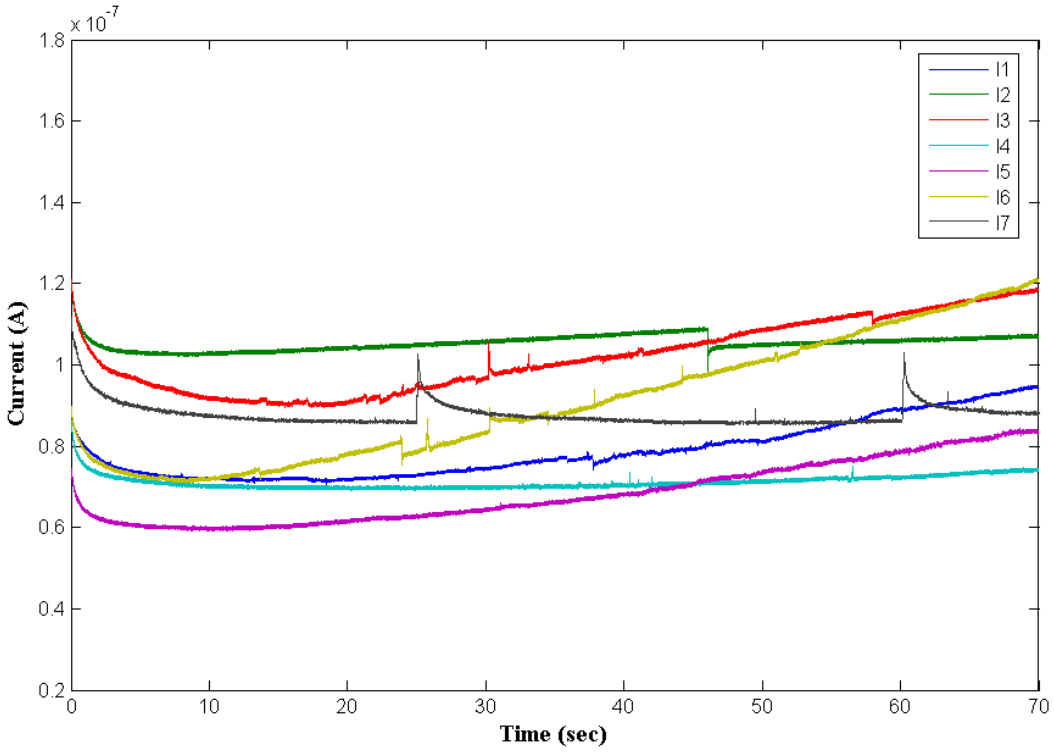

Figure 1-1. Sample of plating current curves, from the electrodeposition of mercury on gold disk-microelectrodes of radius 12.5 µm, under the same experimental conditions. Significant variations and irregularities are remarkable, but not accounted for by the current models.

CHAPTER 2

FUNDAMENTALS AND TIME SCALE ANALYSIS

2.1 Fundamentals of electrochemical amalgam formation

2.1.1) Description of the experimental procedure

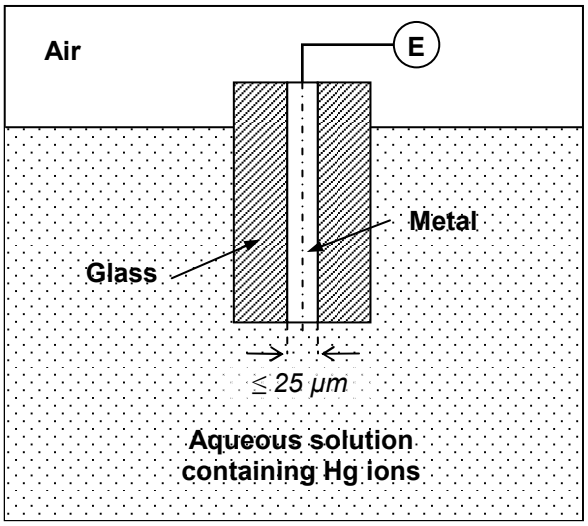

Figure 2-1. Schematic of the system.

Only the half of interest of the system is presented here, but the electrical circuit is closed by a reference electrode.

The SECM microelectrodes are typically formed by melting a metal wire into a glass capillary [5, 8], serving as an electrical isolation coating. The capillary tip is then polished to define a flat electrode, whose diameter is of few micrometers (commonly 5 to 25 μm). The electrode is then submerged into an aqueous solution containing mercury ions with an excess electrolyte, and a lightly negative potential (commonly -0.1V vs SCE or Ag/AgCl) is applied, as

shown schematically in Figure 2-1. This prompts the following reduction reaction at the surface of the electrode, resulting in mercury deposition:

$$Hg_m^{n+} + n\, e^- = m\, Hg \tag{2.1}$$

In eq.(2.1), *m* and *n* define the two different types of involved mercury ions: Hg_2^{2+} (mercury I) or Hg^{2+} (mercury II).

2.1.2) Analysis of the amalgam formation process

As a first step, it is instructive to look carefully at the mercury electrodeposition, and to identify all processes occurring on multitude of time and length scales that may be affect the amalgam formation. It is important to mention here that in this study, the electrodeposition process is assumed isothermal, even if this has not been carefully checked.

Further, to define the scale of interactions, we group all processes into the two main categories: those that occur on a "global" scale given by the size of the electrode, and those that manifest themselves on much smaller (on the order of few nanometers) "local" scale.

Processes at the "global" scale

Two key processes of interest occur at the "global" scale: the mass transfer of mercury ions from the solution bulk to the electrode surface, and the amalgam formation, including droplet growth, morphological adjustment and possibly coalescence phenomena.

Three different phenomena can be responsible for the mass transfer of the mercury ions: migration, which is the transport of ionic species subjected to an electric field; advection, which involves all the species and can be either natural, prompted by a flow due to density gradients, or

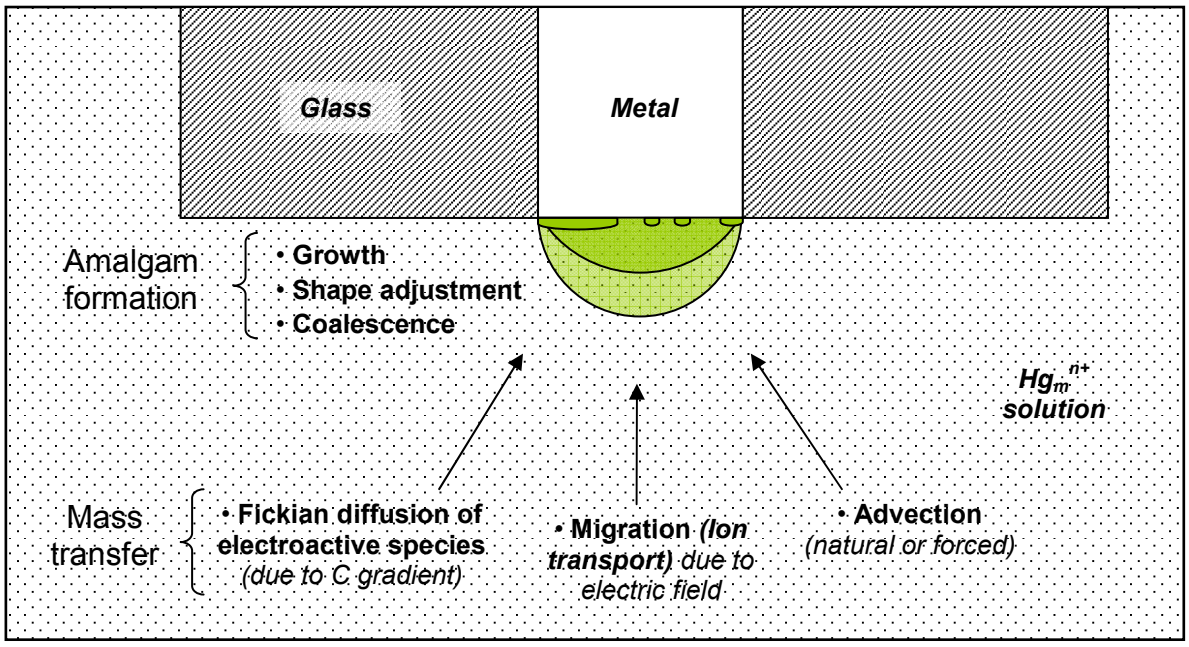

Figure 2-2. Schematic of the processes occurring at the "global" scale.

forced, due to an imposed flow; and finally Fickian diffusion, which is the particles' transfer due to a gradient in their chemical potential, in general, which restricts to a gradient in concentration under certain assumptions.

The other group of processes taking place at the "global" scale concerns with the amalgam formation. The first process to consider is the growth of a mercury droplet on the electrode surface, consequence of the mass flux at its interface induced by the reduction reaction. During the growth, a shape adjustment occurs through the droplet morphology evolution towards the most favorable state. Based on thermodynamic considerations, it corresponds to the lowest energy configuration, which involves a minimum surface area. The last phenomenon playing a role in the formation of the final mercury deposit is the coalescence of separate mercury droplets on the electrode surface. Ion transport and reduction reaction lead the amalgam growth, while the other processes are typically driven by surface energies and contact angle between the different

phases Other phenomena are likely to be involved, including electrostatic interactions, viscosity of the mobile phase and surface diffusion of adsorbed molecules.

Processes on the "local" scale

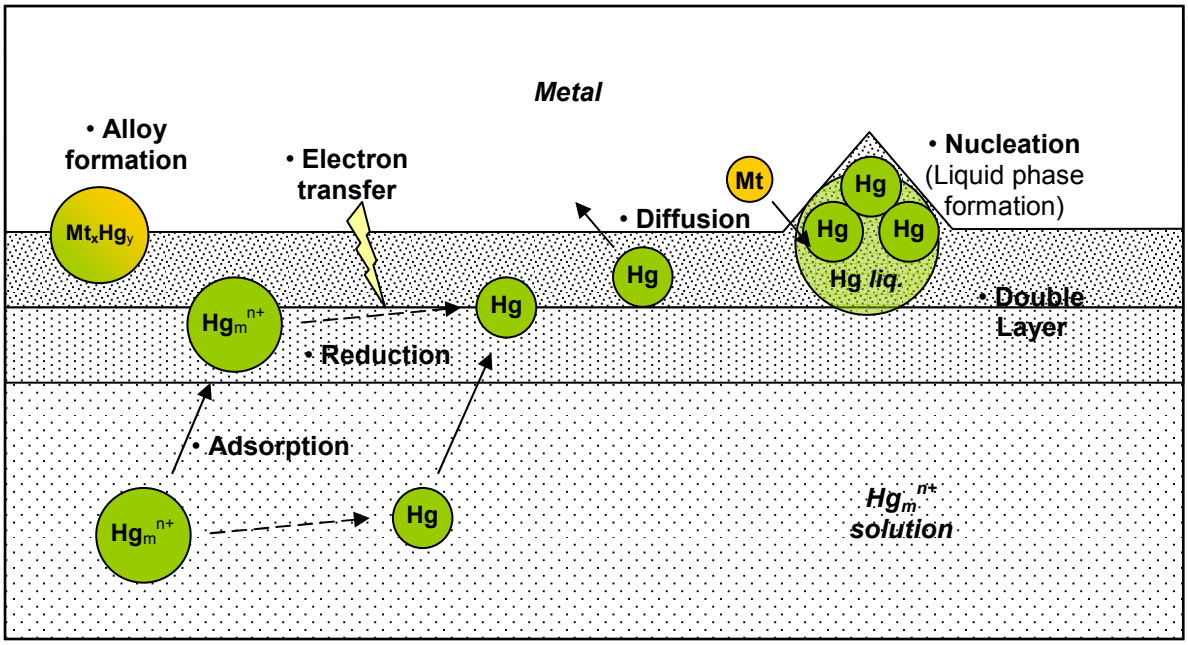

Figure 2-3. Schematic of the processes occurring on the "local" scale.

The processes occurring on the "local" scale include the electrochemical reactions, among which our interest is in reduction of the mercury ions, and the interface phenomena, such as the double layer formation, mercury ion adsorption, the inter-diffusion of mercury and the metal of the electrode, alloy formation, and nucleation.

The "double layer" concept is a model representing the charge accumulation and separation which occur at an electrolyte-electrode interface due to the potential applied [12]. The excess charge on the electrode surface is compensated by an accumulation near the interface of ions of the opposite charge from the solution. This structure, behaving as a capacitor (except that

its capacitance depends strongly on the potential applied on the electrode), causes a potential drop across the layers (see Figure 2-4 below), and may slow down the electrode reaction kinetics. The accumulation of charge on a droplet surface has an influence on its surface tension, which becomes dependent on the applied potential. This phenomenon also results in electrostatic interactions between adjacent droplets which are likely to play a significant role in the coalescence process. The nature of the charge accumulation on the metal (negative or positive) depends on the potential across the interface and the solution composition [12].

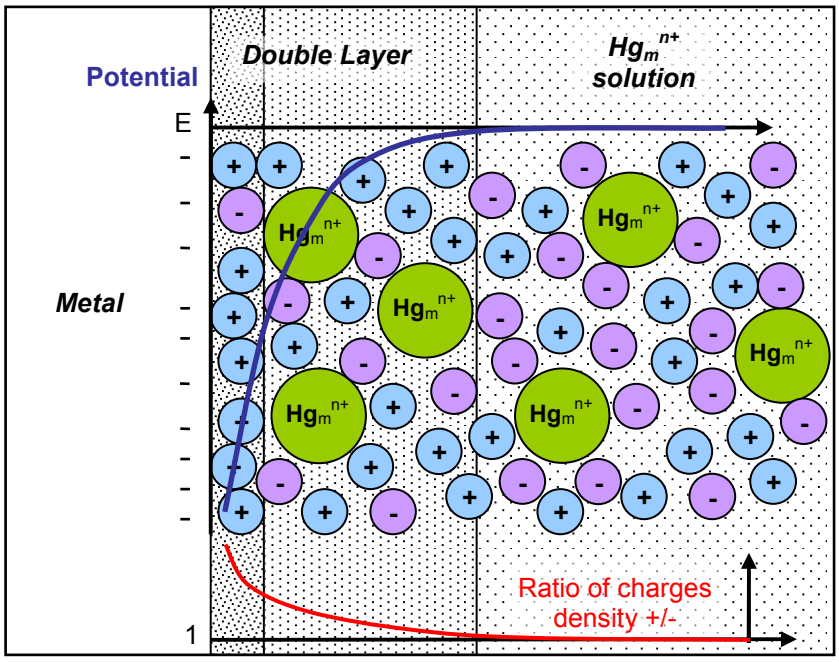

Figure 2-4. Schematic of the electric "double layer".

An excess of negative charges are accumulated on the electrode surface. The first layer is constituted by specifically absorbed positive ions, while the second, the diffuse layer, contains bigger ions that are not specifically absorbed, but distributed such that the electrochemical potential is constant across the layer.

The adsorption is the final step of the mercury ions' transport, and leads to its arrival in an energetically stable position on the surface.

The reduction of the mercury ions takes place close to the surface of the electrode, due to the potential applied (typically -0.1V vs Ag/AgCl [8, 14], giving an overpotential of respectively -0.7 and -0.75V for the redox couples Hg_2^{2+}/ Hg and Hg^{2+}/ Hg). It may occur before or after the adsorption of the ion [12]. The electrochemical reaction involves the transfer of two electrons from the electrode surface to the ion, which may be simultaneous or consecutive [12].

Nucleation is the formation of the mercury liquid phase due to supersaturation, and is more likely to happen on a defect at the electrode surface. Thus, the nucleation rate depends largely on the sites, their types and densities, as well as the applied overpotential [15].

Finally, the contact of mercury and another metal at the electrode interface will lead to phase inter-diffusion phenomena and alloy formation [8-11]. Distinct processes to study are surface (or lateral) diffusion and non-directional diffusion. Also, both diffusion of metal into mercury and of mercury into metal should be considered, even if the first one is usually much faster. These phenomena are limited by the solubility of each phase into the other one.

2.2 Time scale analysis on the "global" scale

Our task here is to determine the limiting process, which defines the amalgam formation rate on the "global" scale. Throughout the time scale study, when numerical values are given, they are computed with the parameters listed in Table 2-1, corresponding to conditions found in applications [5, 8, 13].

Table 2-1. Reference parameters used in numerical analysis.

Parameter	Symbol	Value
Electrode disc radius	A	12.5 μm
Applied potential (vs Ag/AgCl)	E	-0.1 V
Bulk concentration of mercury ions	c^b	10 mM
Diffusion coefficient of mercury ions	D_0	6×10^{-10} m^2/s
Mercury ion type parameter	m	2
Mercury ion valence	n	2
Temperature	T	298 K
Mercury properties		
Atomic mass	M	200.59×10^{-3} kg mol^{-1}
Density	ρ	13.6×10^{3} kg m^{-3}
Viscosity	μ	1.6×10^{-3} Pa s
Surface tension	σ	465×10^{-3} N m^{-1}

2.2.1) Mass transfer

Definition of the problem

The mass transfer of interest here is the process that transports the mercury ions to the electrode surface from the bulk solution (Figure 2-5). The governing equation is a statement of mass conservation:

$$\frac{\partial c}{\partial t} = -\nabla \bullet \vec{J} \tag{2.2}$$

where c denotes the concentration of mercury ions, t the time, $\nabla\bullet$ the divergence operator and $\vec{J}$ the flux of mercury ions. Equation (2.2) needs to be solved for c in order to know at any time the gradient of concentration normal to the electrode surface, which gives the deposition (or plating) current:

$$i(t) = nFD_0 \int_{S(t)} \nabla_n(c) \cdot dS \tag{2.3}$$

where n is the valence of the mercury ion involved, F is the Faraday constant, D_0 is the diffusion coefficient, S is the electroactive surface and $\nabla_n()$ is the surface normal gradient operator.

The initial condition is a steady bulk solution, i.e. uniform bulk concentration of mercury ions everywhere. The boundary conditions for the mercury ions concentration are:

- a constant bulk concentration infinitely far from the electrode surface, assuming that the container used for the experiment is very large compared to the size of the electrode;
- the concentration of mercury ions on the electrode surface is generally determined by the reaction kinetics which depends on the applied electrode potential.

Time scale of electrode kinetics

The net reaction rate for first order reaction is given by [12]:

$$v_{O \to R} = k_f c_O - k_r c_R \tag{2.4}$$

where O and R, respectively, are the oxidized and reduced forms of the redox couple, and k_f and k_r are the forward and reverse rate constants. In our case, O is the mercury ion, Hg_m^{2+}, and R is the neutral mercury molecule, Hg, as described by the reaction equation (2.1). Furthermore, the reaction occurs at the electrode interface, so the surface concentrations are relevant. In the following analysis, we will denote $v_{O \to R}$ by v, c_O by c_{ion}^s and c_R by c_{Hg}^s, to make a distinction between the volumetric (c) and surface (c^b) concentrations. k_f and k_r, are related to the electrical potential by the Butler-Volmer model [12]:

$$\begin{aligned} k_f &= k^o \exp\left(-\alpha f(E - E^{o\prime})\right) \\ k_r &= k^o \exp\left((1-\alpha) f(E - E^{o\prime})\right) \end{aligned} \tag{2.5}$$

where k^o is the standard rate constant, α is the transfer coefficient ranging usually from 0.3 to 0.7 [12], $f = \frac{F}{RT} \approx 38.92\ \text{V}^{-1}$ at 25°C and E and $E^{o'}$, respectively, are the actual and formal electrical potentials. The rate constant is a measure of the kinetic facility of a redox couple, i.e. its "speed" to achieve equilibrium. For mercury ion reduction k^o is of the order of 10^{-2} m/s [12]. The time scale for the reduction reaction, τ_{red}, is then given by:

$$\tau_{red} \sim \frac{\delta x_{red}}{k^0} \tag{2.6}$$

with δx_{red} being a length scale for reduction reaction. The rate limiting step of the reduction, as a multiple step process, may be adsorption or electron transfer. In the absence of detailed knowledge of the microkinetic mechanism, we can conservatively estimate a representative distance for adsorption/desorption to be about 0.5 nm, as this is a typical distance from a surface to the center of an absorbed, hydrated ion [12]. Then, using eq.(2.6), the time scale for the reduction of mercury ions is of the order of 10^{-7} s. We will see based on the next analysis that the reaction is extremely fast as compared to the mass transfer process. Thus, we can assume that, on a "global" scale, the system is always at an electrochemical equilibrium, knows as Nernst equilibrium in electrochemistry. This is a commonly used approximation [8, 12-14], called "infinitely fast kinetics".

The Nernst equation, describing the electrochemical equilibrium, can be written for our case in the following form:

$$\frac{c_{ion}^s}{c_{Hg}^s} = \exp\left(f(E - E^{o'})\right) \tag{2.7}$$

This expression is more general that the Butler-Volmer model, but can be obtained from it assuming v vanishes in eq.(2.4), and then introducing eq.(2.5) and simplifying. The quantity

$(E - E^{o'})$, also called the overvoltage or overpotential, is usually around -0.7V during the mercury plating experiments, as discussed earlier. The concentration of mercury atom at the interface is difficult to estimate, but the molar density of the mercury liquid phase, given by the ratio of the liquid mercury density to its atomic mass, ρ/M, gives an upper bound of the order of 10^4 mol/m^3. Thus, an estimate of the concentration of mercury ions on the electrode surface can be extracted from eq.(2.7). It gives an order of magnitude for c_{ion}^{s} of 10^{-7} mM. This is much smaller than the bulk concentration of mercury ions (10 mM in our reference case), which justifies, in the case of an "infinitely fast kinetics" reaction coupled with a large overvoltage, the assumption that the concentration of mercury ions on the surface of the electrode is vanishingly small.

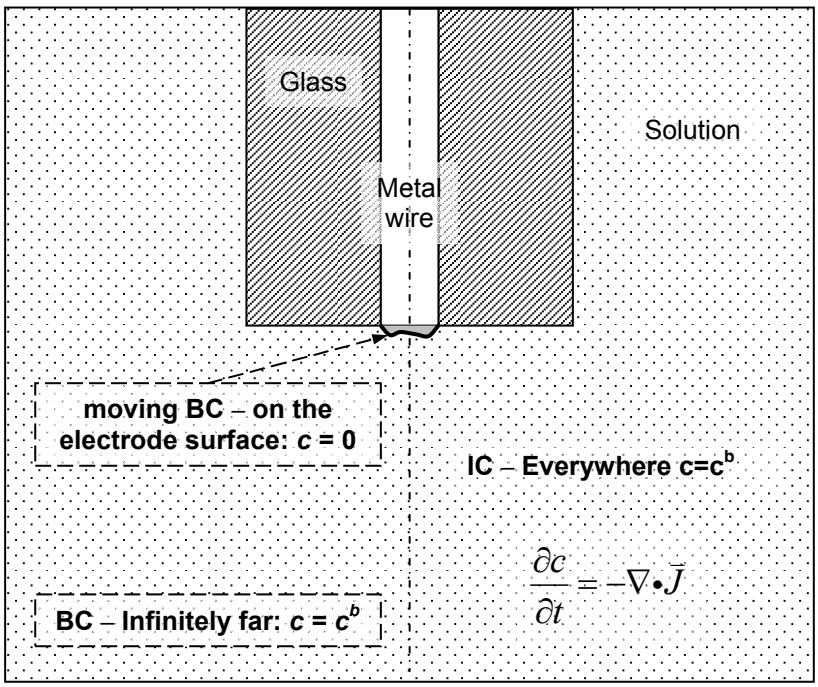

Figure 2-5. General schematic of the mass transfer problem.

BC=Boundary Condition, IC=Initial Condition

c and $\vec{J}$ denote the concentration and flux of the mercury ions, respectively.

Time scales of ion transport

Three processes have to be considered in the evaluation of time scales for mercury ion transport in the solution: diffusion, migration and convection. The expression for the ion flux, $\vec{J}$, accounting for the three transport modes, is [12]:

$$\vec{J} = \underbrace{-D_0(\nabla c)}_{\text{Diffusion}} \underbrace{-\frac{zF}{RT} D_0 c(\nabla \phi)}_{\text{Migration}} \underbrace{+ c\vec{v}}_{\text{Convection}} \tag{2.8}$$

where D_0 is the diffusion coefficient, ∇c is the concentration gradient, $\nabla \phi$ is the potential gradient, z and c are the charge and concentration of the species respectively, and $\vec{v}$ is the velocity of the liquid. The charge is the valence of the ions weighted by the sign of this latter, so in our case: $z = n$. In this formulation, the diffusion coefficient is assumed constant. This assumption will always be made in our analysis for simplicity of argument.

The time scales for the various transport modes are found by considering a scale analysis representation of the mass conservation equation, eq. (2.2):

$$\frac{\Delta c}{\tau} \sim \frac{\Delta J}{\delta x} \tag{2.9}$$

where τ is the general mass transfer time scale and δx is the corresponding length scale.

Convection

It is assumed in our study that there are no convection phenomena, because usually no forced flow is used in plating experiments, and precautions are taken too avoid prompting spontaneous flows: the solution is degassed from O_2 to avoid bubble production, and only a slightly negative potential is applied to prevent the formation of H_2. Thus, no natural convection should theoretically occur during experiments. In fact, the presence of sudden peaks in

experimental plating current data (see Figure 1-1) leads us to suspect bubble generation and some resulting convection; however, we did not pursue the analysis of this phenomenon.

Migration

Migration, caused by a potential gradient, is therefore significant only very close from the electrode surface, in the double layer. This latter is only few nanometers thick, due to the presence of a supporting electrolyte that is always added in excess to the solution to avoid migration. The Debye length, which gives the scale for the double layer thickness, and thus a length scale for the migration phenomenon, is about 1.3 nm [12] in a common case: (1:1) electrolyte with a 0.1M concentration at 25°C [5, 8, 13]. Furthermore, the excess amount of electrolyte coupled with its higher mobility compared to mercury ions makes the supporting ions carry most of the current. This is expressed by the "transference" number, representing the fraction of the total current carried by one given species in the solution [12]:

$$t_i = \frac{|z_i| u_i c_i}{\sum |z_j| u_j c_j} \tag{2.10}$$

with z_i the charge of a species, u_i its mobility and c_i its concentration. The mobility of a species is linked to its diffusion coefficient D_i by the Einstein-Smoluchowski equation [12]:

$$u_i = \frac{|z_i| F D_i}{RT} \tag{2.11}$$

To access the magnitude of an expected transference number for mercury ions, let us now study a simple but representative plating experiment solution: 10mM $Hg_2(NO_3)_2$ with 0.1M KNO_3 supporting electrolyte [8]. This gives a transference number for the mercury ions of:

$$t_i = \frac{4 D_{Hg_2^{2+}} c_{Hg_2^{2+}}}{4 D_{Hg_2^{2+}} c_{Hg_2^{2+}} + D_{NO_3^-} c_{NO_3^-} + D_{K^+} c_{K^+}} \tag{2.12}$$

with $c_{Hg_2^{2+}}$=10mM, $c_{NO_3^-}$=(2×10+100)=120mM and c_{K^+}=100mM. In these conditions, $D_{Hg^{2+}}$ is about 8.3×10^{-9} m^2/s [8], and $D_{NO_3^-}$ and D_{K^+} are of the order of 1.4×10^{-9} m^2/s [16]. This gives a transference number at around 0.1, so the mercury species carries only 10% of the current in the solution.

The migration time scale, τ_{migr} , can be derived from eq. (2.9), concentrating on the contribution of migration to the flux. Assuming the length scale for migration is much smaller than the length scale for diffusion, $\delta x_{migr} \ll \delta x_{diff}$, the resulting balance gives the migration time scale:

$$\tau_{migr} \sim \frac{RT}{nFD_0} \frac{\Delta c \cdot \delta x_{migr}^2}{c \cdot \Delta \phi} \tag{2.13}$$

If we assume Δc of the order of c, $\Delta \phi$ of the order of |E|, and take the Debye length, λ_D , as the migration length scale, δx_{migr} , we obtain an expression for the migration time scale:

$$\tau_{migr} \sim \frac{RT}{nF|E|} \cdot \frac{\lambda_D^2}{D_0} \tag{2.14}$$

Using the parameters of the reference case, the migration time scale is found to be of the order of 10^{-10}s.

Diffusion

The diffusion is due to the concentration gradient induced by the reduction of the mercury ions at the electrode surface. The length scale for this phenomenon is thus given by a characteristic dimension over which the chemical reaction occurs, which is in our case the diameter of the inlaid disc.

The diffusion time scale, τ_{diff}, can also be extracted from eq.(2.9), considering now a balance between the storage (transient) term and the diffusive flux term:

$$\tau_{diff} \sim \frac{\delta x_{diff}^2}{D_0} \tag{2.15}$$

Taking the electrode disk diameter as diffusion length scale, and using the data of the reference case, the diffusion time scale is found to be of the order of 1 s.

Conclusion

Table 2-2. Time- and length- scales for mass transfer* and redox reaction.

Phenomenon	Time scale	Length scale
Convection	Assumed not present	
Migration	10^{-10} s	1.3 nm
Diffusion	1 s	25 μm
Reaction Kinetics	10^{-7} s	0.5 nm

* This values have been established from our reference case.

The magnitudes of the time and length scales for the representative case are summarized in Table 2-2. Diffusion is the only mass transfer process from the bulk solution to the electrode surface, since convection is assumed to be absent and migration is only limited to a very thin layer near the electrode surface. Thus, diffusion is clearly the leading mass transfer process of the mercury electrodeposition.

Comparing the time scale for diffusion to the time scale for the heterogeneous reaction, we see that the mercury ion reduction is extremely fast compared to the mass transfer (7 orders

of magnitude), and the "infinitely fast kinetics" assumption is justified. In conclusion, the mercury electrodeposition itself is a diffusion limited process.

From the time scale analysis, we also see that migration is an extremely fast process compared to diffusion (10 orders of magnitude). Consequently, the double layer, formed through migration, can be considered to be in a quasi-equilibrium state on the time scale of diffusion mass transfer.

2.2.2) Amalgam formation

With an initial concept of the mass transfer process, we study now the amalgam formation, which include three phenomena at the "global" scale: the three-dimensional growth of a mercury droplet on the electrode surface, its morphological evolution to reach a minimum energy configuration, and the coalescence of adjacent islands. As coalescence is not a simple and easily described process, no time-scale has been derived here.

The growth of the deposit is the consequence of the reduction reaction which occurs at its interface with the solution. Indeed, as a metal, mercury is an electrical conducting medium, and thus a droplet laying on the surface of the electrode constitutes an extension of this latter. As we seen earlier, the reaction rate is limited by the ion transport, which occurs through diffusion. Thus, the growth time scale, τ_{growth}, is given by the diffusion process:

$$\tau_{growth} = \tau_{diff} \tag{2.16}$$

Now, we need to derive a length scale for the droplet growth. This will be done in a planar case, but the spherical problem has been found to give a similar result. The linear flux of mercury ions, per unit area, J'', induced by diffusion at the droplet surface, is obtained by applying eq.(2.8) to the limited case:

$$J'' = D_0 \left(\frac{\partial c}{\partial x} \right)_s \tag{2.17}$$

where x is the problem space coordinate, with the corresponding axis pointing from the solution towards the deposit layer. It is related to the growth rate, v_{growth}, which is the thickness of the layer deposited per unit time:

$$v_{growth} = \frac{nM}{\rho} J'' \tag{2.18}$$

where n is the valence of the mercury ions involved, M is the corresponding molar mass and ρ is the mercury liquid phase density. Now, for the purpose of scale derivation, the growth rate, due to diffusion, can be expressed as the ratio of the growth length scale, δx_{growth}, over the diffusion time scale:

$$v_{growth} \sim \frac{\partial x_{growth}}{\tau_{diff}} \tag{2.19}$$

Moreover, the mercury ions concentration gradient at the interface can be formulated by the difference in concentration between the solution bulk and the deposit surface over the diffusion length scale. Since we justified earlier that the electrode concentration can be assumed equal to zero, this gives:

$$\left(\frac{\partial c}{\partial x} \right)_s \sim \frac{c^b}{\partial x_{diff}} \tag{2.20}$$

Introducing eq. (2.17), (2.19) and (2.20) in eq. (2.18) and extracting δx_{growth} , it yields:

$$\partial x_{growth} = \frac{nMD_0 c^b}{\rho} \frac{\tau_{diff}}{\partial x_{diff}} \tag{2.21}$$

Finally, we simplify using the relation between the time and length scale for diffusion derived in eq.(2.15):

$$\partial x_{growth} = \frac{nMc^b}{\rho} \partial x_{diff} \tag{2.22}$$

With the numerical values of our reference case, listed in Table 2-1, we obtain a ratio of the growth length scale over the diffusion one of the order of 10^{-4}.

Looking on the global scale, the driving process for the morphological adjustment of the deposit is surface relaxation (the evolution of droplet surface to reach the optimum, i.e. energetically most favorable configuration, shown schematically in Figure 2-6). One can distinguish two different events, driven by the pressure difference in the mercury liquid phase between the actual configuration and the optimum one (see Figures 2-6 and 2-7): the move of the contact line over the metal electrode surface to relax the edge of the droplet (we will call it spreading surface relaxation); and the other dealing with the surface adjustment aside from the edge (we will call it free surface relaxation).

The corresponding time scales will be obtained by combining a term of the governing equation for fluid motion, also known as the Navier-Stokes equation, with the Young-Laplace equation, which describes the pressure increase across a curved interface. In reality, the move of the contact line over the electrode surface is a very complex process, depending also on phenomena at the "local" scale, like surface diffusion, electrostatic and Van der Waals forces. Here, we restrict the problem to a simple process, slowed by the liquid mercury viscosity, in order to obtain an estimate for the time scale.

The Navier-Stokes equation is:

$$\underset{\{1\}}{\frac{\partial v}{\partial t}} + \underset{\{2\}}{(v \cdot \nabla)v} = \underset{\{3\}}{-\frac{1}{\rho}\nabla p} + \underset{\{4\}}{F} + \underset{\{5\}}{\frac{\mu}{\rho}\nabla^2 v} \tag{2.23}$$

where v is the fluid velocity, p its pressure, ρ the density and μ the dynamic viscosity. The different terms correspond to the effect of : {1}- acceleration, {2}- advection of momentum, {3}- hydrodynamic pressure force, {4}- external body force and {5}- viscous stress.

The Young-Laplace equation to consider is:

$$\Delta p = \sigma \cdot \Delta k_m \tag{2.24}$$

where Δp is the pressure variation over the process, Δk_m the corresponding mean curvature variation of the surface, and σ the surface tension of liquid mercury in aqueous solution. As stated earlier, Δp is in our case the pressure difference in the mercury liquid phase between the actual configuration and the optimum one. For the purpose of time scale derivation, the corresponding mean curvature variation can be approximated by the curvature of the optimal surface.

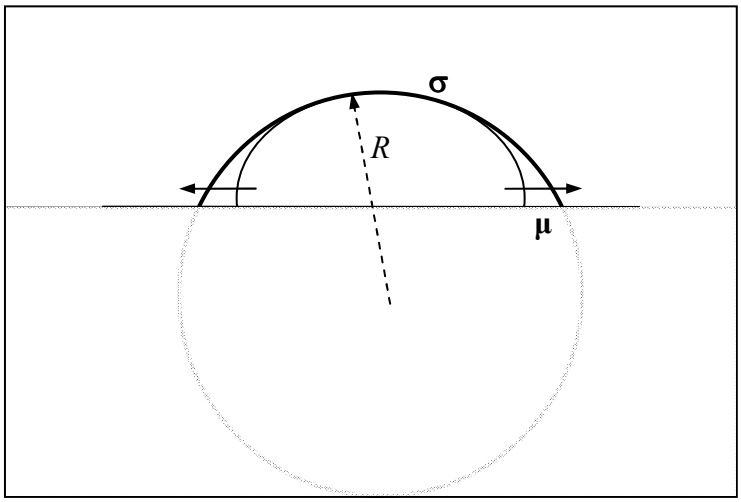

Figure 2-6. Schematic of the surface spreading relaxation.

The spreading surface relaxation time scale, τ_{Srel} , is obtained in the case of negligible inertia (assumption discussed in next section), by balancing the terms {3} and {5} of the Navier-Stokes equation (2.23), and introducing the Young-Laplace equation (2.24). This balance gives:

$$\frac{\Delta p}{\delta x} \sim \mu \frac{\Delta v}{\delta x^2} \tag{2.25}$$

with δx the length scale of the phenomenon. Then, Δv is approximated by $\delta x/\tau_{Srel}$, and the Young-Laplace equation, eq. (2.24) is used to obtain the pressure scale. The resulting estimate of the spreading surface relaxation time scale is:

$$\tau_{Srel} \sim \frac{\mu}{k_m \cdot \sigma} \tag{2.26}$$

with μ the dynamic viscosity, k_m the mean curvature and σ the relevant surface tension. In the amalgam formation study, we are interested in finding upper bounds for the time scales of the processes, in order to find out if they can approach the mass transfer, i.e. diffusion, limiting time scale. For the scale analysis, we treat the viscosity μ and the surface tension σ as constants, even though in reality σ is slightly dependent on the potential applied. Consequently, we want to define a minimum for the mean curvature k_m. This latter is of the order of $1/R$, with R the radius of curvature of the droplet's surface, so we need to establish a maximum for this value, which can virtually be infinite (case of a flat layer). If we consider that it is reached by a sphere-cap in "penned" configuration over the largest microdisk of interest (a=12.5 μm), with a height of 1 μm ("global" scale minimum range), it gives a sphere radius of around 80 μm (see sphere-cap geometry in Appendix). Introducing this in eq.(2.26), and using the values of mercury properties given in the nomenclature, it gives an upper bound for the spreading surface relaxation time scale of the order of 10^{-7} s.

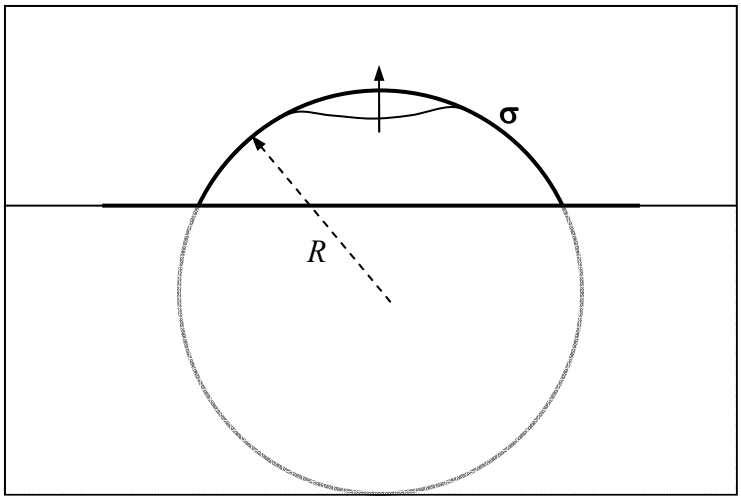

Figure 2-7. Scheme of the surface free relaxation.

The free surface relaxation time scale, τ_{Frel} , is derived, still in the case of negligible inertia, by balancing the terms {1} and {3} of the Navier-Stokes equation (2.23):

$$\frac{\Delta v}{\tau_{Frel}} \sim -\frac{1}{\rho}\frac{\Delta p}{\delta x} \tag{2.27}$$

with δx the length scale of the phenomenon. Then, Δv is approximated by $-\delta x/\tau_{Frel}$, and τ_{Frel} is extracted, which yields:

$$\tau_{Frel} = \sqrt{\frac{\rho \cdot \delta x^2}{\Delta p}} \tag{2.28}$$

Finally, we introduce the Young-Laplace equation, eq. (2.24) and we obtain an estimate of the free surface relaxation time scale:

$$\tau_{Frel} = \delta x \cdot \sqrt{\frac{\rho}{k_m \cdot \sigma}} \tag{2.29}$$

with ρ the density, k_m the mean curvature, σ the surface tension and δx the length scale of the surface movement. As explained earlier, we want to find an upper bound for this time scale. As the surface tension σ and the density ρ are constants, we need to establish a maximum for δx and

a minimum for k_m. This latter has been estimated earlier to 1/80 μm^{-1}. The maximum length scale for the surface movement can be taken as the electrode disc diameter, $2a$, for the largest microdisc of interest (a=12.5 μm). This gives, using eq.(2.29) and the values of the mercury properties given in the nomenclature, an upper bound for the free surface relaxation time scale of the order of 10^{-6} s.

Table 2-3. Time and length scales for deposit growth due to diffusion and surface relaxation processes *.

Phenomenon / Data	Time scale	Length scale
Diffusion	1 s	25 μm
Deposit growth	1 s	2.5×10^{-3} μm
Radius of curvature		80 μm **
Surface spreading relaxation	10^{-7} s **	
Surface free relaxation	10^{-6} s **	25 μm **

* This values have been established from our reference case.
** This values are upper bounds.

This analysis shows us that the surface relaxation phenomena are much faster than droplet growth and limiting mass transfer process, diffusion, by at least six orders of magnitude. Consequently on the time scale of the ion transport processes, mercury proceeds through a sequence of thermodynamically optimum shapes, that can be predicted via quasi-equilibrium calculations. Therefore, we can conclude that looking at the "global" scale, and under our specific conditions (notably large overpotential, neglecting advection and in presence of an excess electrolyte), the electrodeposition of mercury on a metal microelectrode is a fully diffusion-limited process.

2.2.3) Note on long range forces

We have not evoked the long range forces yet, but naturally one should wonder about the influence of an external electrostatic field or gravity. The former perturbation, which may have a significant effect, is cancelled by doing the experiment in a Faraday cage, which insulates the setup from external electrostatic fields. But gravity is still acting, and one can wonder if it can lead to droplet detachment or deformation.

Let us first study the possibility of a droplet detachment. The force due to gravity on a mercury droplet (i.e. the weight) is:

$$W = \rho V \cdot g \tag{2.30}$$

with ρ the density of mercury, V the volume of the droplet and g the acceleration due to gravity. At this point and to be exact, the force due to the pressure exerted by the solution on the droplet should be taken into account. But it depends largely on the droplet configuration, and is anyway very small, because of the low water density compared to mercury, and the low depth of the experiment (only a few centimeters, which gives a pressure of the order of 100 Pa). In order to establish an upper bound of the weight, let us consider a volume equivalent to the one of a sphere of radius equal the radius of the largest inlaid disk of interest (a = 12.5 μm). This gives, with the values for the constants given in the nomenclature, a weight of the order of 10^{-9} N.

The weight of the droplet will be counterbalanced, in the case of interest where the droplet is pendant, by the cohesion force, which can be derived by differentiating the cohesion energy with respect to a characteristic length:

$$C = \frac{\partial}{\partial r}\left(\pi r^2 \cdot \gamma_{ms}\right) = 2\pi r \cdot \gamma_{ms} \tag{2.31}$$

if we consider a circular interface area, with r its radius and γ_{ms} the specific interfacial energy between the mercury and the substrate (here the electrode metal). This latter is of the order of

0.36 N/m [17]. Now, we need to estimate the interface size. As, a priori, the metals used for the electrode are more mercurophilic than hydrophilic (because otherwise the mercury would not stay on the surface), overgrown droplets can only be formed if the inlaid disc is fully covered. So r is taken as the disk radius of the electrode considered in the weight computation. This gives a cohesion force of the order of 10^{-5} N. This is much greater (4 orders of magnitude) than the weight, so if we consider only reasonably grown droplets, a detachment is not likely to happen. A similar study has been done by Cazabat [18].

Let us now study the possibility of a deformation of the droplet due to gravity. The pressure exerted by gravity on a droplet surface point can be defined by:

$$\Delta p_g = \rho g h \tag{2.32}$$

with ρ the density of mercury, g the gravity and h the height of mercury on top of the surface point considered. An upper bound of this pressure can be established considering a reasonably overgrown configuration ($h = 2a$) over the largest electrode disc of interest (a = 12.5 μm). This gives a pressure exerted by gravity on the droplet's surface of the order of 1 Pa.

This pressure is counterbalanced by the one exerted by the surface tension. This latter is given by the Young-Laplace equation (2.24):

$$\Delta p_t = \sigma \cdot k_m \tag{2.33}$$

with k_m the mean curvature ($2/R$ for a sphere) and σ the relevant surface tension. A minimum for the former value has been established in the previous chapter to 1/80 μm^{-1}. This gives a lower bound for the pressure exerted by the surface tension of the order of 10^3 Pa. This is still three orders of magnitude greater that the maximum pressure due to gravity, so this latter is not likely to deform the droplet.

To conclude, if we limit the study to reasonably grown droplets (radius not bigger than the electrode disc diameter), which is the case, gravity can be neglected. The same conclusions have been reached by Colyer and Oldham et al. [13, 19].

CHAPTER 3

MODELING OF THE ELECTRODEPOSITION PROCESS

3.1 Basic hypotheses and overall model

Using the time-scale analysis of the processes at the "global" scale, the first model of mercury electrodeposition is developed, based on the general problem presented in 1.2.a) (see Figure 3-1). The following assumptions and simplifications have been made:

1- only the transport of the mercury ions is considered

2- the electrodeposition is a diffusion limited process, with no other mass transfer processes involved

3- all non-diffusion processes are either infinitely slow (frozen/quasi-steady) or infinitely fast (quasi-equilibrium)

4- the reduction reaction is infinitely fast and, due to a large overpotential, the concentration of mercury ions on the electrode surface is zero

5- the inlaid disk is imbedded into an infinite, non-conducting plane (insulation)

6- the inlaid disk is entirely covered by a single mercury film from the first time step

7- the amalgam has a sphere-cap shape

The justification of assumption 1 comes from the fact that migration is neglected which eliminates the coupling between the mercury ion concentration and the concentrations of the other species present in the solution. The next three assumptions (2-4) come directly from the conclusions of Chapter 1. Assumption 4 makes the Dirichlet boundary condition on the electrode surface homogeneous. Assumption 5 can be met experimentally by making the radius of the

glass capillary much larger that the one of the inlaid disc (at least ten times) [20]. Assumption 6 is made due to the simplicity it imparts to the problem, and its impact will be discussed later. We noticed from experiments that this configuration, called the "penned" configuration, is reached during the plating process after a variable transient time. This delay depends mostly on the size and metal type of the electrode, and the concentration of mercury ions, given a constant potential. Finally, assumption 7 stems from an assumption of a uniform surface tension combined with the assumption of a quasi-equilibrium shape. The lowest energy configuration (equilibrium) is that of minimum surface area which is the sphere segment or sphere-cap.

The result of the list of assumptions is the following idealized model for the diffusion limited growth of the amalgam electrode. The governing equation is a statement of mass conservation during mass transfer of mercury ions, operated by diffusion:

$$\frac{\partial c}{\partial t} = D_0 \nabla^2 c \tag{3.1}$$

where c is the concentration of mercury ions and D_0 is the diffusion coefficient. The boundary conditions of the problem are:

$$c \to c^b \text{ far from the electrode} \tag{3.2}$$

$$\nabla_n c = 0 \text{ on non-conducting surface} \tag{3.3}$$

and

$$c = 0 \text{ on electrode surface} \tag{3.4}$$

where c^b is the bulk concentration and $\nabla_n c$ is the projection of the concentration gradient on the surface normal vector. The initial condition is:

$$c = c^b \tag{3.5}$$

The geometry of the electrode surface (i.e. amalgam surface) is obtained through mass balance of the deposition process. The net instantaneous current at the electrode surface is:

$$i(t) = nFD_0 \int_{S(t)} \nabla_n(c) \cdot dS \tag{3.6}$$

where S is the electrode/solution interface. Equation (3.6) is integrated in time to obtain the net charge passed due to electrodeposition, Q :

$$Q = \int i \cdot dt \tag{3.7}$$

which can be related to the net mercury deposited using:

$$V = m \cdot \frac{M}{\rho} \cdot \frac{Q}{nF} \tag{3.8}$$

where V is the mercury amalgam volume, and M and ρ are, respectively, the atomic mass and the density of liquid mercury. The volume V together with the electrode disk radius a determine the mercury deposit interface shape, under the assumptions of a sphere-cap geometry and "penned" configuration. The equations used to relate the various geometric parameters in Figure 3-1 are listed in Appendix.

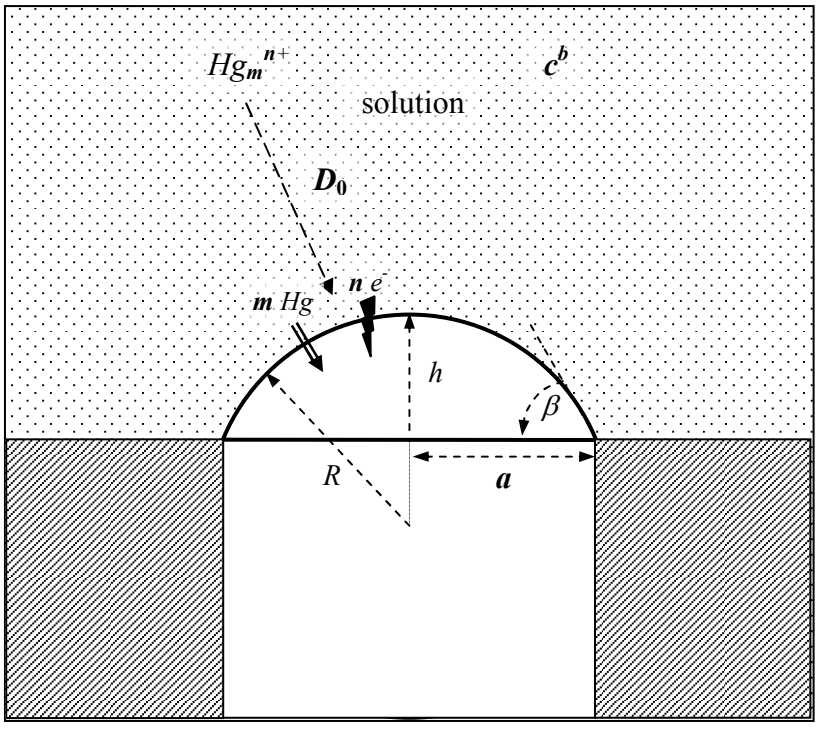

Figure 3-1. Schematic of the analyzed process.

At this point, it is relevant to mention that eq.(3.6) gives only the current due to the mercury electrodeposition, and thus neglects the current generated by the charging of the double-layer (see description in Chapter 2). The sign of this capacitive current is given, on the amalgam surface, by the difference between the potential applied at the electrode and the electro-capillary maximum (ecm). The electro-capillary maximum is the potential for which the measured surface tension of the interface between the body and solution will be greatest, which corresponds to the situation where no charge is accumulated on the surface. For mercury in an aqueous solution, the ecm is about -0.480 V vs NCE [17]. This is lower than the range of potentials typically applied (about -0.1V vs NCE), and thus the charge accumulated on the metal side will be positive, corresponding to a deficiency of electrons. Consequently, during the double-layer formation, a transient non-faradaic current flows counter to the faradaic deposition current. As the amalgam grows, the area of its interface with the solution increases, delaying the end of the double-layer charging. But based on the time-scales established in Chapter 2, migration, driving the double-layer formation, is extremely fast compared to the amalgam growth, and thus the charging can be considered instantaneous. An order of magnitude for the charge involved in the double-layer formation can be obtained from the charging equation [17]:

$$Q_{DL} = C_{DL} E \tag{3.9}$$

where C_{DL} is the double-layer capacitance, and E the applied potential versus ecm. The double-layer capacitance can be estimated by $C''a^2$, where C'' is the capacitance per unit surface area (typically of the order of 0.1 F/m^2 [17]) and a is the radius of the electrode. Under the experimental conditions of the reference case described in Table 2-1, this gives a charge of the order of 10^{-5} μC, negligible compared to the charge passing through the electrode interface due to mercury electrodeposition (see data presented next).

3.2 Experimental data

In order to test the models derived using the above assumptions, results are compared to two different kinds of data. The first kind consist of long time charge curves, which allow one to validate the gross accuracy of the electrodeposition model by checking the evolution of the volume deposited. The volume of mercury deposited is given by the accumulated charge involved in the plating (eq.(3.8)). The total charge is obtained experimentally by integration of the plating current over the time elapsed since the beginning of the potential step, i.e., through application of eq.(3.7). As this data is an integration of a direct measurement, it is less sensitive to small perturbations. The second kind of data is plating current curves. As the current is directly measured during the experiment, it is very sensitive to any perturbation, and thus exhibits a lower repeatability. However, its analysis is essential to discerning details of what is happening on the electrode at any time, and thus to obtaining a deeper understanding of the electrodeposition process. For the purpose of checking our models, it allows us to immediately see the biggest flaws.

Table 3-1. Experimental / simulation parameters of the reference data.

Parameter \ Source	Colyer et al. "**Data 1**"	Rudolph "**Data 2**"
Electrode disc radius a	0.5, 1, 2.5, 5, 12.5 µm	12.5 µm
Electrode metal	Pt	Pt, Au
Ion's type parameter m (n=2)	1	2
Diffusion coefficient D_0	8.3×10^{-10} m^2/s	6×10^{-10} m^2/s
Bulk concentration	5 mM	10 mM
Electrolyte concentration	10 mM	0.1 M
Applied potential (vs NHE)	0.097 V	0.141 V
Experiment sample interval	60 s	1 to 10 ms

Data with two different origins were used: experimental and theoretical charge curves for inlaid platinum (Pt) discs of different radii from Colyer, Luscombe and Oldham [13], which are denoted "Data 1"; and some experimental plating current curves of inlaid platinum (Pt) and gold (Au) discs of radii 12.5µm, from Douglas Rudolph and co-workers (Professor Mizaikoff's group, School of Chemistry and Biochemistry at Georgia Tech), that constitute "Data 2". The corresponding experimental / simulation parameters are given in Table 3-1.

3.2.1) Charge curves

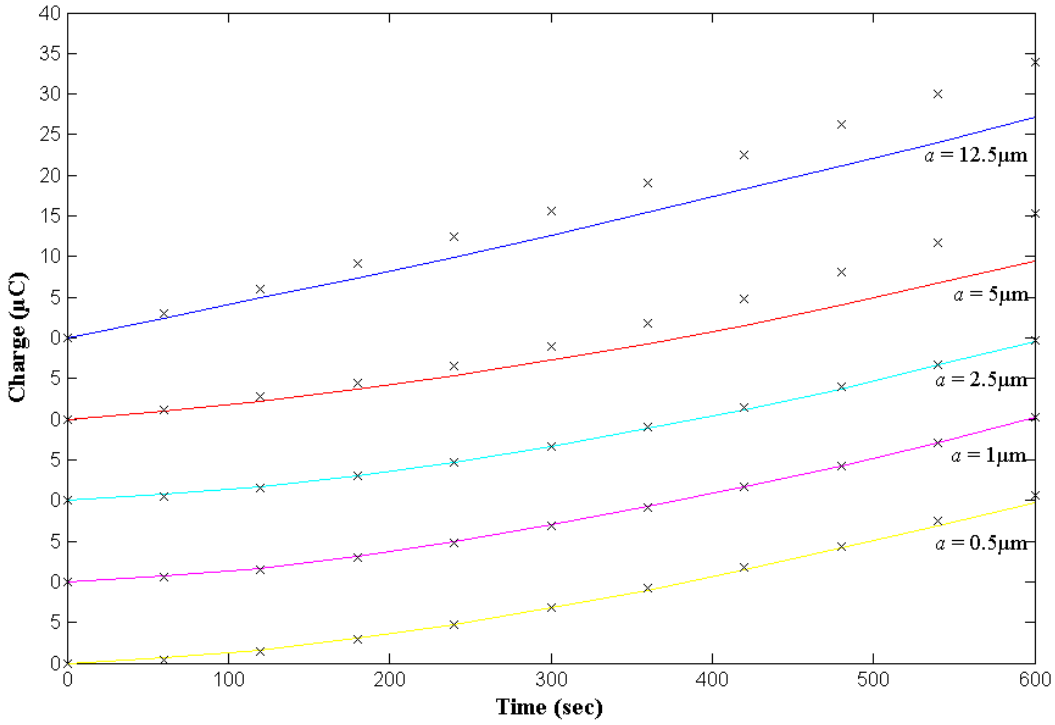

Figure 3-2. "Data 1": Charge curves reproduced from Colyer, Luscombe and Oldham (1989).

*"*The theoretical (curves) and experimental (asterisks) dependence upon time of the faradaic charge during the diffusion-controlled electrodeposition of mercury from a 5.0 mM aqueous solution of mercuric ion onto inlaid platinum discs of the stated radii.*"* [13]

The reference charge curves have been obtained from a 1989 paper by Colyer, Luscombe and Oldham [13]. Their data and simulation results are presented in Figure 3-2. The precise experimental conditions are detailed in the paper, and the main parameters are listed in Table 3-1. Each experimental point on the figure is the average from six experiments carried out under identical conditions, with "background correction". The theoretical curves have been computed under the basics assumptions presented earlier, using a model that will be discussed later. These results will allow us primarily to check the correctness of our model implementation, since, using the same assumptions, the computed curves should be quite close. One advantage of this set of data is to provide reliable experimental curves. Another is, by providing corresponding theoretical curves, to show the current state of the art of mercury electrodeposition modeling. Furthermore, the results, being for a range of disc radii, provide us with some information not available using only the results provided by our collaborators at the Georgia Institute of Technology.

3.2.2) Current curves

The reference current curves are experimental plating data produced on request by Douglas Rudolph and co-workers (Professor Mizaikoff's group, School of Chemistry and Biochemistry at Georgia Tech) [21]. No correction of any kind has been made, and the experiments have not been optimized. Only the "cleanest" datasets have been retained here, as the purpose is to test our first models, which assume ideal conditions. Thus, we do not include here some curves that exhibit extremely noisy or erratic behavior. The experimental conditions are identical to the ones presented in details in Ref. [5], and the main parameters are listed in Table 3-1.

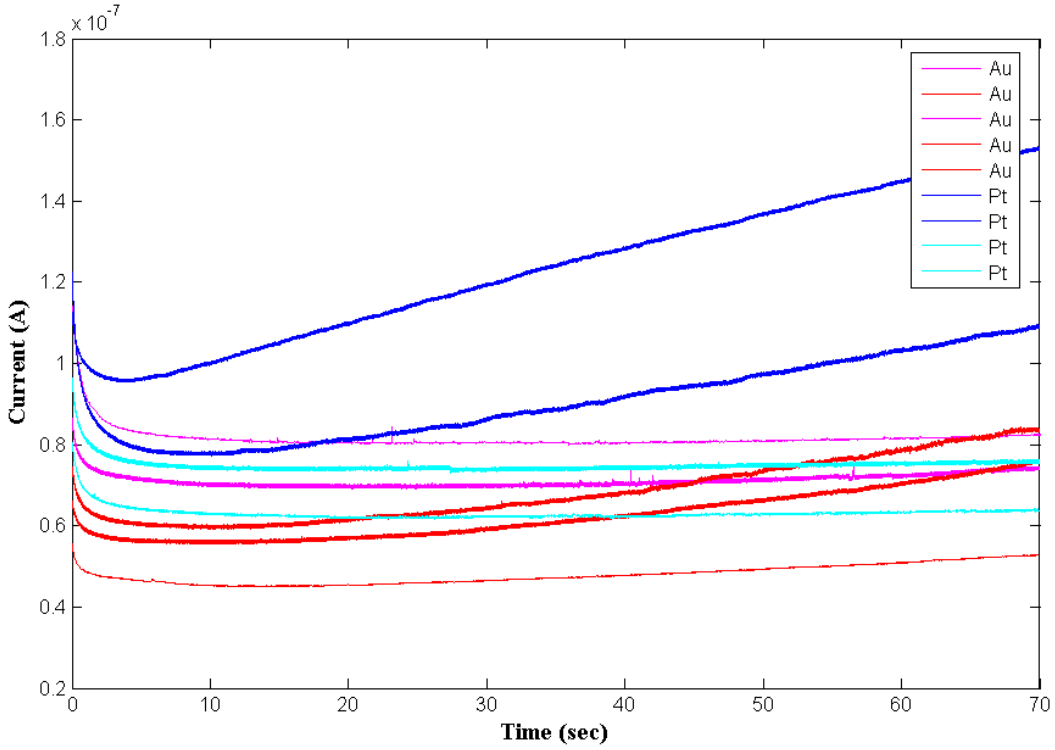

Figure 3-3. "Data 2": Experimental plating current curves, from the electrodeposition of mercury on platinum (Pt) and gold (Au) inlaid disks of radius 12.5µm (for detailed plating conditions, see Table 3-1).

Figure 3-3 presents short experiments all carried out under the same conditions, except for the electrode disc metal, which is either gold (Au) or platinum (Pt). Two things are particularly striking: the current's magnitude is rather variable from the very beginning, and the slopes of the curves are also not all similar. The results are divided into two categories: the ones with very low slope are designated using light colors, and the ones that demonstrate a significant increase rate are represented in darker colors. The reasons for the different behaviors, highlighted in Figure 3-3, is not obvious This set of curves shows the variety as well as the range of the plating currents at short electrodeposition times.

3.2.3) Experimental difficulties

The plating experiment is not a fully mastered process. It involves many parameters, some known, whose roles are understood, some known, but whose influence is not explained, and probably others that are unknown. Furthermore, some are known but difficult to control. Among them, the exact size and geometry of the electrode is one of the more problematic. Indeed, the fabrication process is very sensitive to the specific procedure and experience of a person, and a small change in the electrode disc geometry can significantly change its behavior. Furthermore, the inlaid disc surface is affected by each experiment, and thus it is impossible to carry out two experiments with an identical electrode geometry and surface. Among the more common problems encountered, there is a recess of the inlaid disk due to the polishing process, or a deviation from a perfectly circular shape. Others parameters may include the freshness of the solution, which can change its exact composition, as can variability in the degassing process. The roughness of the electrode surface may also play a role.

3.3 Model 1: Quasi-steady-state

3.3.1) Justification of the quasi-steady-state approximation

In the literature, several models have been derived based on the problem presented in section 1.2, but mostly for electrodes of fixed geometry, not complicated by the difficulty of a moving boundary. For instance, in the case of disc or hemisphere microelectrodes, the current reaches its steady-state value, or comes very close to it, after a short transient period [4], that may be neglected or not, depending mainly on the size of the electrode and the deposition time. The transient current is mainly due to the formation of the diffusion layer, caused by the consumption of the ionic species at the electrode surface, and the time for the ions in the bulk to

travel to this latter due to diffusion. In the case of a disc, the time for the current to reach its steady-state value within ε percents, $\tau_{ss}(\varepsilon)$ can be estimated by [4]:

$$\tau_{ss}(\varepsilon) = 10^4 \frac{4a^2}{\pi^3 \varepsilon^2 D_0} \tag{3.10}$$

with a the radius of the disc and D_0 the diffusion coefficient. Equation (3.10) shows that the duration of the transient period is strongly dependent on the size of the electrode; the dependence is the same for a hemisphere [4]. Using $D_0 = 7\times10^{-10}$ m^2/s (an average of the experimental data reported in Table 3-1), we obtain $\tau_{ss}(5) \approx 12$s for a=12.5µm, $\tau_{ss}(5) \approx 2$s for a=5µm and $\tau_{ss}(5) <$ 0.1s for a=1µm. Thus, the transient period may be significant only for the larger electrodes, and in the case of short experiments (less than about 300s).

These numerical criteria are strictly valid only for a disk electrode, which is a good approximation of the problem during the "early growth" encompassing spreading and/or merging of the first mercury deposits (in a form of thin film) over the electrode disc surface until the "penned configuration" is reached. But we do not know yet what is the duration of this early growth, we can just assume that it strongly depends on the electrode size. After this period, the growth in height of the amalgam may delay or even prevent the diffusion layer (and thus the current) from reaching a steady-state. Precisely, it would be a quasi-steady-state, meaning that at any time, the situation is very close to the steady state corresponding to the "frozen geometry". Preventing the achievement of this state is the fact that the growth of the amalgam is constantly changing the electrode surface, and thus the area and the location of the interface boundary condition (see Figure 3-4, and eq. (3.4)).

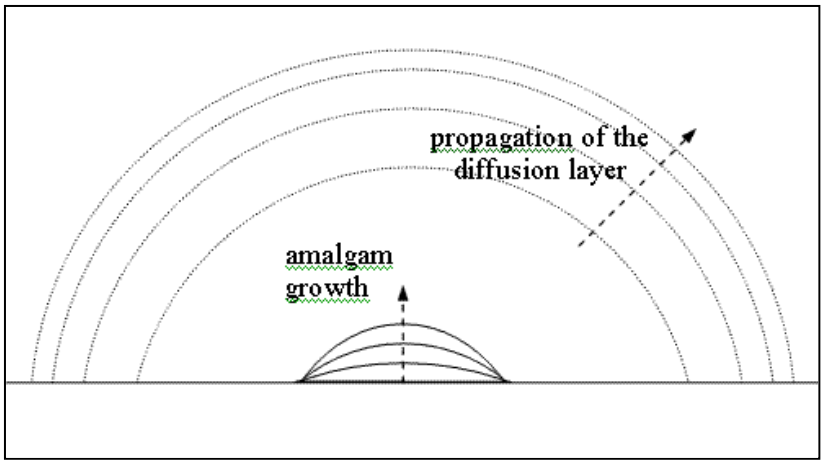

Figure 3-4. Schematic of the diffusion layer's formation problem.

Based on the derivation of time and length scale for the deposit growth as linear diffusion limited process (Chapter 2, eq.(2.16) and (2.22)), the ratio of the growth rate, v_{growth} (in this case deposit thickness increase rate), over the diffusion layer expansion rate, v_{diff}, is given by:

$$\frac{v_{growth}}{v_{diff}} = \frac{nMc^b}{\rho} \tag{3.11}$$

For an usual bulk concentration of mercury ions (c^b=10mM), this gives a ratio of the order of 10^{-4}. Thus, the deposit interface expansion is much slower than the diffusion layer boundary propagation, due to the huge disparity (about three orders of magnitude) in mercury atom density between the liquid phase, dense phase of mercury atoms, and the aqueous solution, dilute phase which is providing the atoms to the other. So we can reasonably expect that a quasi-steady-state will be reached quickly.

3.3.2) Modeling of the quasi-steady-state current

Using the assumptions described in section 2-1 and the quasi-steady-state approximation, the model presented in section 2-1 is modified by replacing eq. (3.1) with:

$$\nabla^2 c = 0 \tag{3.12}$$

in which the transient (storage) term is neglected. An approximate and general expression for the resulting steady-state current, i_{ss}, has been derived by Myland and Oldham [14]:

$$i_{ss} \approx nFD_0 c^b \sqrt{2\pi A} \tag{3.13}$$

where n is the valence of the mercury ions present in the solution, c^b is their bulk concentration and A is the area of the amalgam electrode/solution interface.

Equation (3.13) is accurate to within 10% for all oblate hemispheroidal microelectrodes, and for prolate hemispheroidal microelectrodes while the height, h, is less than 6.3 times the base radius, a [14]. Moreover, for a sphere-cap electrode, this margin of error is always valid, whatever the size, and it even falls to 2% when $h > a$. Equation (3.13) provides an upper bound of the current to a fixed sphere-cap, being exact only for a hemisphere, and thus it leads to an overestimate of the quasi-steady current, especially at the very beginning. Unfortunately, a correction coefficient, $\alpha(h/a)$, which gives the exact solution for a sphere-cap electrode [14], is not convenient for use in simulations:

$$\alpha(h/a) = \sqrt{\frac{2}{1+(h/a)^2}} \int_0^\infty \frac{\cosh\{\omega \arctan(h/a)\}}{\cosh\{\omega \operatorname{arccot}(h/a)\}\cosh\{\pi\omega/2\}} \mathrm{d}\omega \tag{3.14}$$

Initially, the idealized electrode geometry is a disk. The exact steady-state solution to the diffusion problem to an inlaid disk of radius a (under the assumptions listed in 2.1) is given by [22]:

$$i_{ss,disk} = 4nFD_0 c^b a \tag{3.15}$$

Using eq.(3.13) with A the area of the disk, $A=\pi a^2$, gives $i_{ss} = \sqrt{2}\pi nFD_0 c^b a$. The ratio $\frac{i_{ss}}{i_{ss,disk}} = \sqrt{2}\pi/4 \approx 1.11$, so eq. (3.13) introduces an initial 11% error, predicting a higher initial current. Nevertheless, the steady-state approximation being itself an underestimation of the current in early times, since the transient current due to the formation of the diffusion layer is neglected, this approximation will be considered reasonable and the initial current will be computed using equation (3.13) with the area of a disk.

3.3.3) Simulation algorithm

In this section the base routine of the first mode, "Model 1," is presented. The model parameters are a, the radius of the electrode disc, m and n, defining the mercury ion in presence (see eq.**(2.1)**, in fact m defines the mercury ion, as n=2 in both cases considered), D_0, the diffusion coefficient, c^b, the bulk concentration of mercury ions, Δt, the increment time step and t_{end}, the total plating time. The algorithm is the same as the one used by Colyer et al. [13] to compute the theoretical charge curves composing "Data 1", except that the correction coefficient introduced in the last section has been neglected in our model. The amalgam electrode shape and rate of growth is therefore calculated approximately by using the following procedure.

Starting with initial conditions,

A = area of the disc = πa^2

V *(volume)* = 0

the following series of steps is performed:

I – Computation of the current (according to eq.(3.13)):

$$i = nFD_0 c^b \sqrt{2\pi A}$$

II – Computation of the charge entering:

$$\Delta Q = i \cdot \Delta t$$

III – Computation of the new volume:

$$V = V + m \cdot \frac{M}{\rho} \cdot \frac{\Delta Q}{nF}$$

IV – Computation of the new shape:

$$K = \left(\pi^2 (3V + \sqrt{a^6 \pi^2 + 9V^2})\right)^{1/3} \quad \text{and} \quad h = -\frac{a^2 \pi}{K} + \frac{K}{\pi}$$

$$\text{then} \quad R = \frac{a^2 + h^2}{2h} \quad \text{and} \quad A = 2\pi \cdot R \cdot h$$

V – Increment the time and loop to step I, unless $t = t_{end}$.

3.3.4) Results and analysis

Charge and current plating curves were computed from "Model 1" for comparison with the curves from the corresponding experimental conditions of "Data 1" and "Data 2". The time step used for the computations is 6s for the charge curves and 1s for the current curves, with an initial computation at t=1s. The time step and initial time independence of the results has been checked.

Figure 3-5 shows us many interesting things. First, the charge curves computed from our model, "Model 1", are almost identical to those computed by Colyer et al. [13], except for the case of the largest disc radius, a = 12.5μm, and even in this case, they are quite close. This suggests that our model is correctly implemented and that the current correction coefficient, $\alpha(h/a)$, is relevant only for the largest radius. This observation is bolstered by recalling the fact that the error introduced by neglect of $\alpha(h/a)$ is maximum (10%) at the very beginning, when

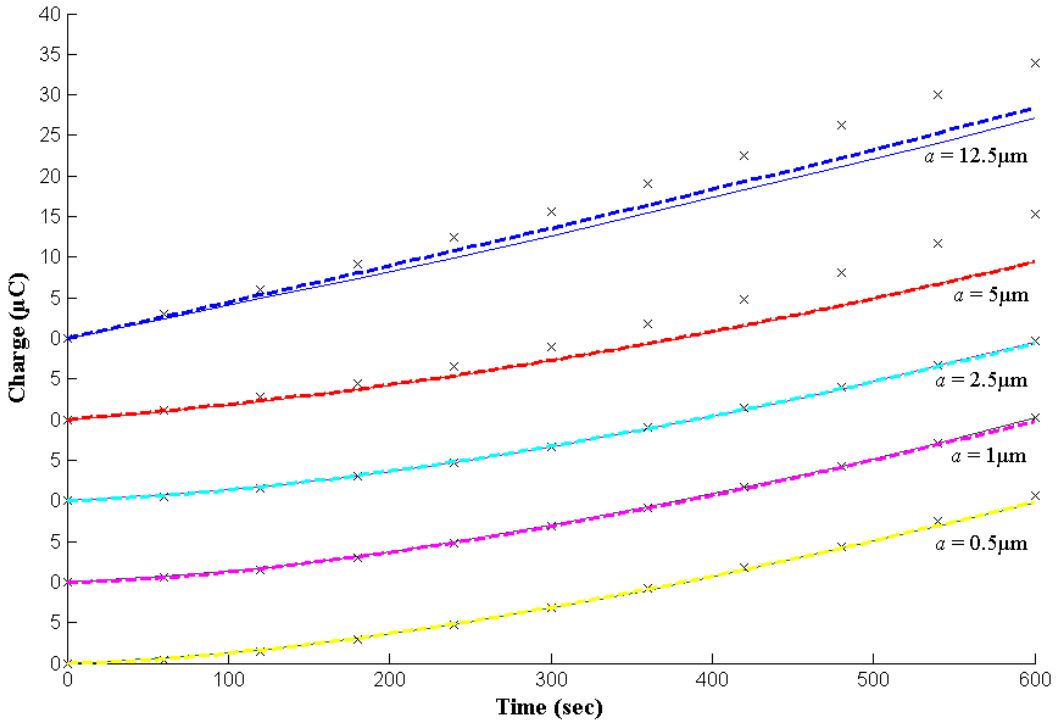

Figure 3-5. Theoretical charge curves from "Model 1" (- -) and "Data 1" (–), and experimental data from "Data 1" (×), for different disk radii *a*.

the amalgam is almost a disc (h/a small), decreases to zero for a hemispherical shape (h/a=1), and for later growth (h/a>1) is very limited (2%). Looking at the amalgam evolution for the different radii (Figures 3-6 and 3-7), we see that the ratio of the height of the amalgam over its base radius h/a stays under 1 during a significant time only in the case of the largest disc radius, a = 12.5µm. Thus, we can conclude that under experimental conditions similar to the ones of "Data 1", and for disc radii equal or less than 5µm, the correction coefficient can be neglected if the precision required is not too high (error up to around 0.5µC acceptable). The curve for a=12.5µm shows us the cumulative effect with time, due to the fact that the charge is obtained by integration. While the error on the current, due to the negligence of the correcting coefficient, is maximum at the beginning, its influence on the charge curve is notable only after an

accumulation with time. Since our current approximation is an upper bound, the charge curve from “Model 1” is logically higher than the one from the model of Colyer et al..

Also from Figure 3-5 we see that the theoretical charge curves match perfectly the experimental ones for the smallest disc radii, but that the models are not satisfactory for the two largest ones (a=12.5 and 5 μm), although the discrepancy is not too large. This suggests that the assumptions made for the derivation of the model are fair, but we are neglecting something that mainly affects the largest sizes considered. As previously mentioned, an error on a charge curve is due to the accumulation of an earlier error on the current. Furthermore, the current, which is the instantaneous slope of charge curve, is dependent on the area of the electrode, which increases through the accumulation of mercury atoms. Since these latter are products of the reduction reaction, the amount deposited is proportional to the charge passed through the interface, and thus the charge curve slope is dependent on the value of the charge. This coupling renders difficult the comparison of charge curves after long times if a significant error is present at earlier times. The only obvious conclusion from the theoretical and experimental charge curve comparison for the two larger disc radii is that a phenomenon, increasing the current compared to its quasi-steady-state expression in early times, is not taken into account by the models. As a result of the charge curves for smaller disc radii, we know in addition that this phenomenon depends on the electrode size, and is almost negligible for disc radii equal or smaller than 2.5μm. Colyer et al. [13] suggest that this phenomenon is the diffusion layer formation process, during which the current will be higher than the quasi-steady-state prediction. This transient effect is indeed likely to be the explanation, since it occurs in the early times, lead to an increase of the current compared to its steady-state value and is strongly dependent on the size of the electrode [4].

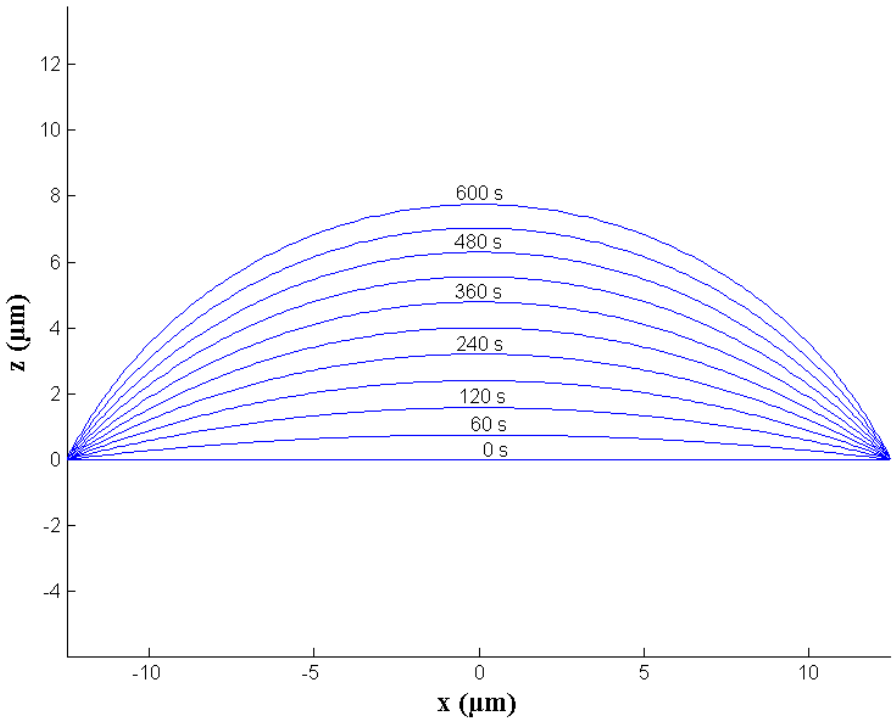

Figure 3-6. Amalgam shape at different plating times, computed from "Model 1" and corresponding to the charge curve from "Data 1" for a disk radius of a = 12.5 µm.

Figures 3-6 and 3-7 displays the amalgam shape evolution and growth corresponding to the charge curves presented in Figure 3-5. They show that the smaller the initial electrode size, the faster the amalgam reaches an over-hemispherical configuration. This leads the smaller electrodes to reach very overgrown configurations, with a ratio of h/a as high as 28 for the 1µ-radius electrode after 600s. This raises questions about the influence of gravity on the shape of these amalgams, but such configurations are not of practical interest since the utility of a small electrode is its size, so there is no point to cover it with a comparatively much bigger amalgam droplet: these particular cases have been made only for analysis purposes. Figures 3-6 and 2-7 also allow us to rudimentarily check the validity of the growth rate scale derived in Chapter 2. The growth for the 12.5µm electrode is about 8µm in height in 600s, which gives an average rate

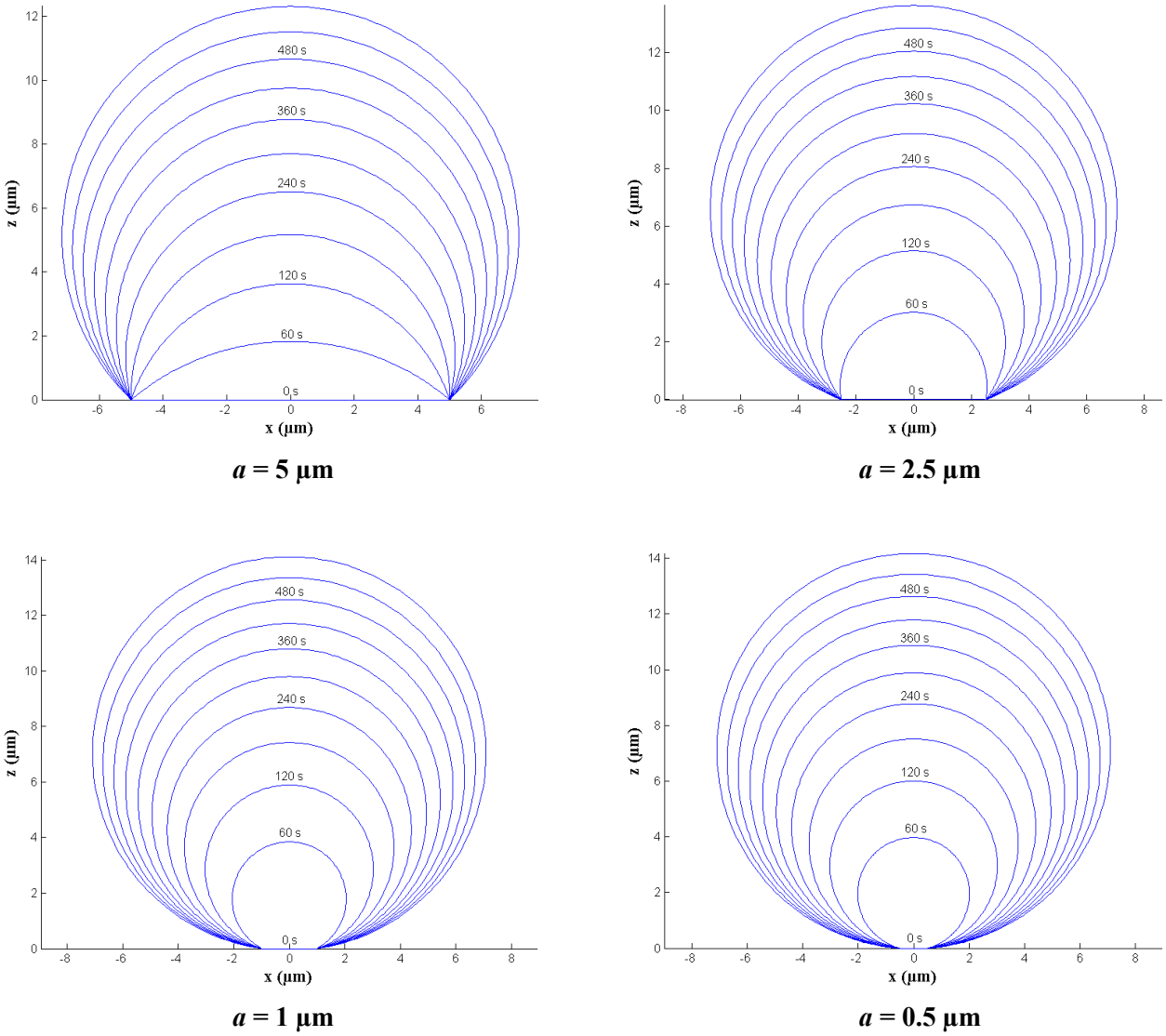

Figure 3-7. Amalgam shape at different plating times, computed from "Model 1" and corresponding to the charge curves from "Data 1" for disk radii of 5, 2.5, 1 and 0.5 µm.

of around 10^{-8} m/s. This is of the order of the value found earlier, 2.5×10^{-9} m/s, presented in Table 3-3, and logically higher, since edges and curvature, both increasing the diffusion to the deposit, are not accounted for in the linear scale derivation. The corresponding diffusion layer propagation rate, about 10^{-5} m/s based on Table 2-3, is still three orders of magnitude higher than

the amalgam growth rate. Consequently, the quasi-steady-state approximation seems pretty reasonable.

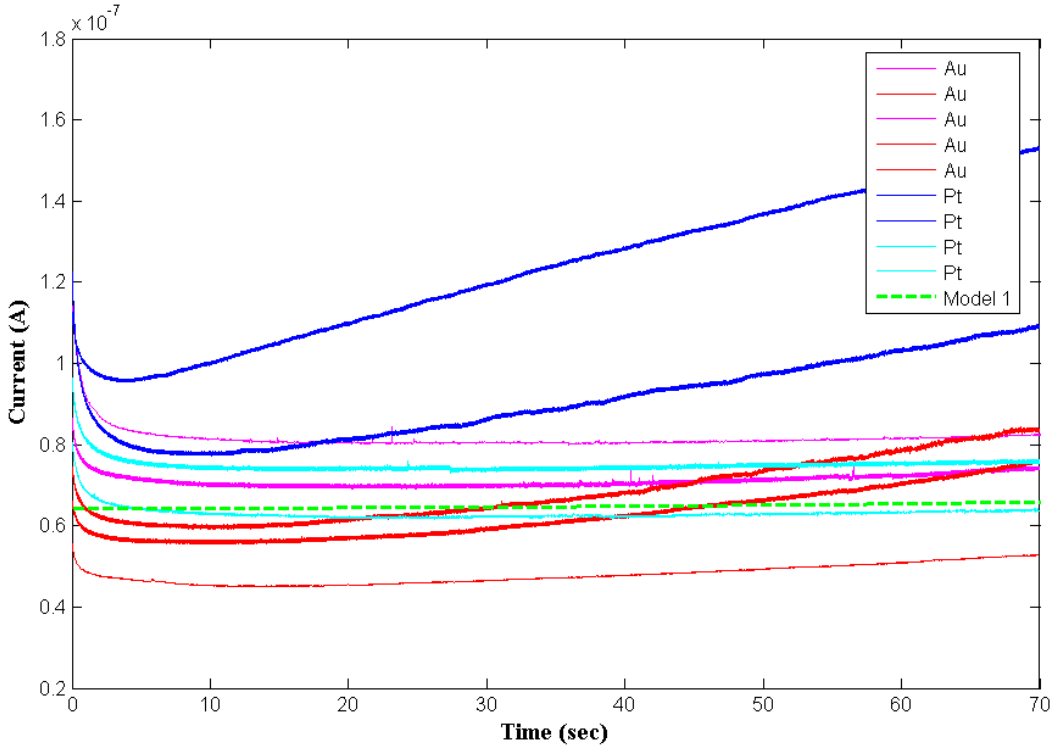

Figure 3-8. Plating current curves for disk radius of 12.5 µm : experimental data with gold (Au) or platinum (Pt) electrodes from "Data 2"; and theoretical curve computed using the same conditions with"Model 1".

From the analysis of the current curves for a disk radius of 12.5µm (Figure 3-8), we first notice that there is indeed a transient current at the very beginning of the process that we may have to take into account. Its magnitude is decreasing very fast, and it seems to represent a notable contribution to the total current only during the first 15s, which may be nevertheless significant for short plating experiments.

As discussed earlier, the plating current data can be split into two kinds of current evolution after the transient period: a constant and significant increase, or a comparatively

negligible current increase. From Figure 3-8, we see that our model predicts the second kind of evolution. As we do not know the reasons for this behavioral discrepancy, we cannot tell if our model is fully satisfactory. Nevertheless, it shows that the model accounts for one characteristic evolution type, validating for this case the assumptions made. In the other case, the slope of the curves is much higher, reflecting probably a faster growth of the amalgam. Concerning the magnitude of the current, our model is in the range of the experimental data, although somewhat low.

3.4 Model 2: Long-time transient

3.4.1) Modeling and analysis of the transient current

From the comparison of the simulation based on the "Model 1", using a steady-state current expression, with the plating current curves of "Data 2", we noticed that a high but rapidly decreasing transient current was present at the beginning of the electrodeposition process, but neglected in our modeling. Thus we need an expression to account for this transient current.

In the literature, the transient current modeling is split into two periods: short-time transient and long-time transient. The former is limited to the very early times, because it assumes that the current density is a local property, depending only on the geometry of the electrode in the immediate vicinity of the point considered, and not on the electrode global shape [23]. This approximation is useful while the diffusion layer does not extend significantly from the electrode surface. The range of applicability can be estimated using the diffusion "length" [23, 24], whose order of magnitude is given by [12]:

$$\delta_{diff} \sim \sqrt{D_0 t} \tag{3.16}$$

with D_0 the diffusion coefficient of the species consumed at the electrode surface and t the time from the beginning of the potential step. This relation is derived in the case of a planar diffusion. The short-time transient period corresponds to $\delta_{diff} < a$, with a a characteristic dimension of the electrode so, using eq.(3.16), this transient period encompasses times such that $t < \tau_{diff} \sim \frac{a^2}{D_0}$. In contrast, the long-time transient period starts when the diffusion layer becomes dependent only on the global geometry of the electrode, i.e. for $\tau_{diff} \sim \frac{a^2}{D_0} < t$. The simple approximation of the transition between these two periods is a current research issue [24, 25].

During the very earliest times, the geometries of interest for our case (inlaid disc progressively coated by mercury) are a disk and sphere-caps with low height. The short-time transient current response to a large potential step, under the same general assumptions as in the previous model (essentially: diffusion-limited process, infinitely fast kinetics and amalgam modeled by a sphere-cap laying on an infinite insulating plane) can be given by the series [23]:

$$i_{short-time} = nFc^b D_0 \left[A\left(\frac{1}{\sqrt{\pi D_0 t}} + \frac{1}{R} \right) + \ldots \right] \tag{3.17}$$

where R is the radius of the sphere-cap, which is a function of the parameters h and a (see Appendix), and t is the time elapsed since the beginning of the potential step. The first term of this series is the well known "Cottrellian current":

$$i_{cottrell} = nFc^b A\sqrt{\frac{D_0}{\pi t}} \tag{3.18}$$

It is evanescent, accounting for the diffusion layer formation. The second term, constant, is the "prompt current". This latter is generally induced by "edges or curvatures effect" [23]. For a

disc, the relation is the same as eq.(3.17) except that the second term in the parentheses is 1/*a*. This term being constant, it is interesting to compare it to the steady-state current. In the case of a sphere-cap, the ratio is found using eqs. (3.13), (3.17) and the sphere-cap geometrical relations given in Appendix:

$$\frac{i_{prompt}}{i_{ss}} \approx \frac{A/R}{\sqrt{2\pi A}} = \sqrt{1-\cos\beta} \tag{3.19}$$

where A is the area of the sphere-cap, R is the radius and β is the contact angle. This is an approximation since the expression used for the steady-state term is not exact (see 2.3.b)). Nevertheless, it shows that the prompt current is always lower than the steady-state current with this formulation, and the difference is very significant when β is small. For a disk, the ratio is:

$$\frac{i_{prompt}}{i_{ss}} = \frac{A/a}{4a} = \frac{\pi}{4} \approx 0.79 \tag{3.20}$$

with a the radius of the disk, so the prompt current is about 20% lower than the steady-state one with this formulation.

For the long-time transient current formulation, we are interested in the cases of the disk and oblate sphere-caps inlaid on an insulated plane (since we can assume that by the time the amalgam reaches a hemispherical configuration, the transient is negligible). For the disk case, an accurate expression has been derived by Shoup and Szabo [26], from an original asymptotic expansion by Aoki and Osteryoung [27] (still under the same assumptions listed in 2.1):

$$i_{long-time} = 4nFD_0c^b a\left[A_1 + A_2\tau^{-1/2} + A_3\exp(-A_4\tau^{-1/2})\right] \tag{3.21}$$

with $A_1 = \pi/4$, $A_2 = \pi^{1/2}/4$, $A_3 = 1 - A_1$, $A_4 = (A_2 - 2\pi^{3/2})/A_3$ and $\tau = D_0t/a^2$. This formulation is very accurate, since the maximum error induced for all times is around 0.6% [26]. When $\tau >> 1$ (i.e. $t >> \tau_{diff}$), this expression can be developed to an asymptotic solution:

$$i_{long-time} = 4nFD_0c^b a\left[1+\frac{a}{\pi^{3/2}\sqrt{D_0 t}}+...\right] = nFD_0c^b\left[4a+\frac{8}{\pi^2}A\sqrt{\frac{D_0}{\pi t}}+...\right] \quad (3.22)$$

This expression has been derived differently by Phillips [28], with a supplementary term. It is interesting to notice that the first term of the relation is the steady-state current, while the second is the "Cottrellian current" weighted by $8/\pi^2 \approx 0.81$.

To our knowledge, no fully explicit formulation has been derived for the long-term transient current to a sphere-cap. An asymptotic expression ($t >> \tau_{diff}$) for oblate hemispheroids is given by Rajendran [25] based on the work from Phillips [28]:

$$i_{long-time} = 4nFD_0c^b a\left[\frac{\pi}{2}l_0+\frac{\sqrt{\pi}}{2}l_0^2\frac{a}{\sqrt{D_0 t}}+...\right] \quad (3.23)$$

with $l_0 = \frac{\sqrt{1-\omega^2}}{\mathrm{Arccos}(\omega)}$ and $\omega = \frac{h}{a}$ l_0 can be approximated by $\frac{2}{\pi}+\left(1-\frac{2}{\pi}\right)\omega$ with an error of less than 1% over [0,1]. The above formulation can be rewritten to make explicit the steady-state current and the "Cottrellian current":

$$\begin{aligned} i_{long-time} &= nFD_0c^b\left[k(\omega)\cdot\sqrt{2\pi A}+k^2(\omega)\cdot A\sqrt{\frac{D_0}{\pi t}}+...\right] \\ \text{with } k(\omega) &= \sqrt{\frac{2}{1+\omega^2}}\cdot l_0 \end{aligned} \quad (3.24)$$

The function $k(\omega)$ ranges from 0.9 at ω=0 to 1 for ω=1. Thus, the first term of the relation (3.24) stays within 10% of our formulation of the steady-state current to a sphere-cap (3.13); and the second term within 20% of the "Cottrellian current".

To conclude, whether we consider the short-time or long-time transient period, the current can always be modeled by the sum of the steady-state current and the "Cottrellian current", with an error in most cases lower than 20% compared to the specific formulations.

Moreover, this margin decreases as the ratio h/a rises to h/a=1. We have not studied the prolate configurations, because the transient current will be negligible compared to the steady-state component by the time these are reached. One can notice that the short-time transient period is negligible under the conditions of our experimental data, since the time scale for diffusion, τ_{diff}, is at most 1s, corresponding to the larger electrode (based on eq.(2.15)).

As discussed in the previous section, the models studied, all developed for non-growing electrodes, are accurate in our case only if the growth of the amalgam is much slower than the diffusion layer formation. As a result from the above analysis, we decide to use the "Cottrellian current" for the transient part, $i_{transient}$, of the current formulation:

$$i_{transient} \approx nFc^b A\sqrt{\frac{D_0}{\pi t}} \tag{3.25}$$

The complete expression for the current is now:

$$i \approx \underbrace{nFc^b D\sqrt{2\pi A}}_{\text{Steady state}} + \underbrace{nFc^b A\sqrt{\frac{D}{\pi t}}}_{\text{Transient}} \tag{3.26}$$

Equation (3.26) defines "Model 2" and is incorporated using the same routine as that used for "Model 1."

3.4.2) Results and analysis

In this section, the charge and current plating curves computed from "Model 2" are compared to the ones from "Model 1" and the experimental data, "Data 1" and "Data 2", under matching experiment conditions. The time step used for the computations is 6s for the charge curves and 1s for the current curves, with an initial computation at t=1s. The time step and initial time independence of the results has been checked.

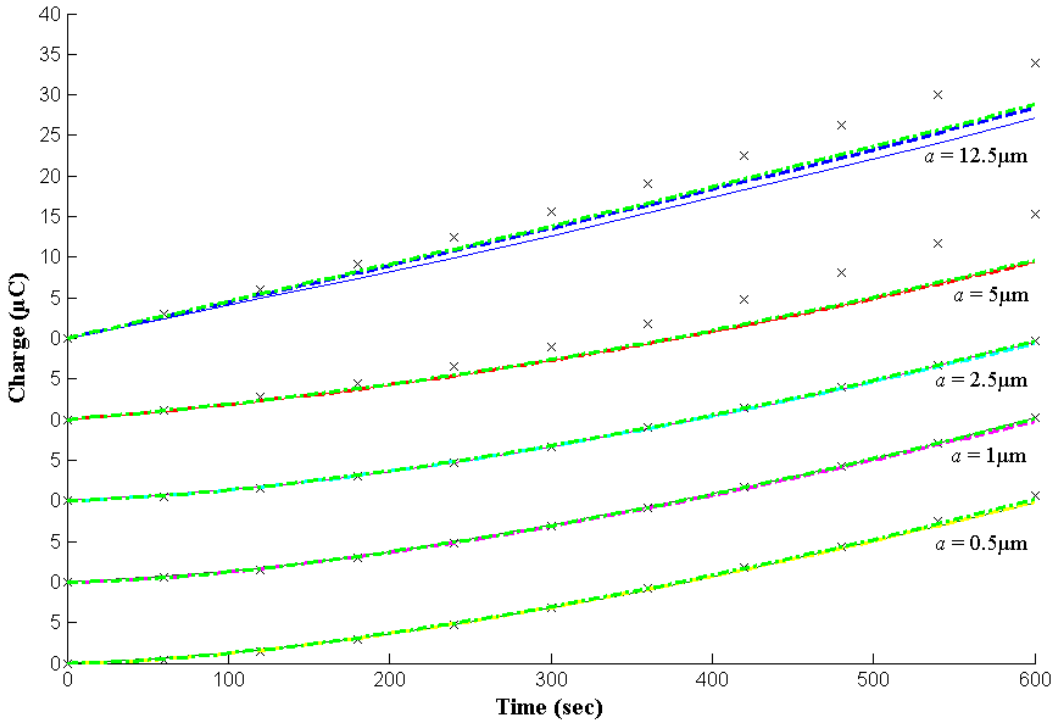

Figure 3-9. Theoretical charge curves from "Model 2" (− · − *green*), "Model 1" (- -) and "Data 1" (–), and experimental data from "Data 1" (×), for different disc radii *a*.

From Figure 3-9, we see that the addition of the transient current term does not significantly affect the charge curves, although a slight increase is noticeable. Indeed, the charge curve from "Model 2" is above the one from "Model 1", but the difference is very small. This means that either the transient current approximation is too low, or that the explanation for the difference between the theoretical and experimental data lies within the quasi-steady-state term.

Figure 3-10 presents the relative increase of the charge deposited due to the addition of the transient current term, in the theoretical curves presented in Figure 3-9. This has been plotted by computing the relative discrepancy between the charge curves from "Model 2" and "Model 1".

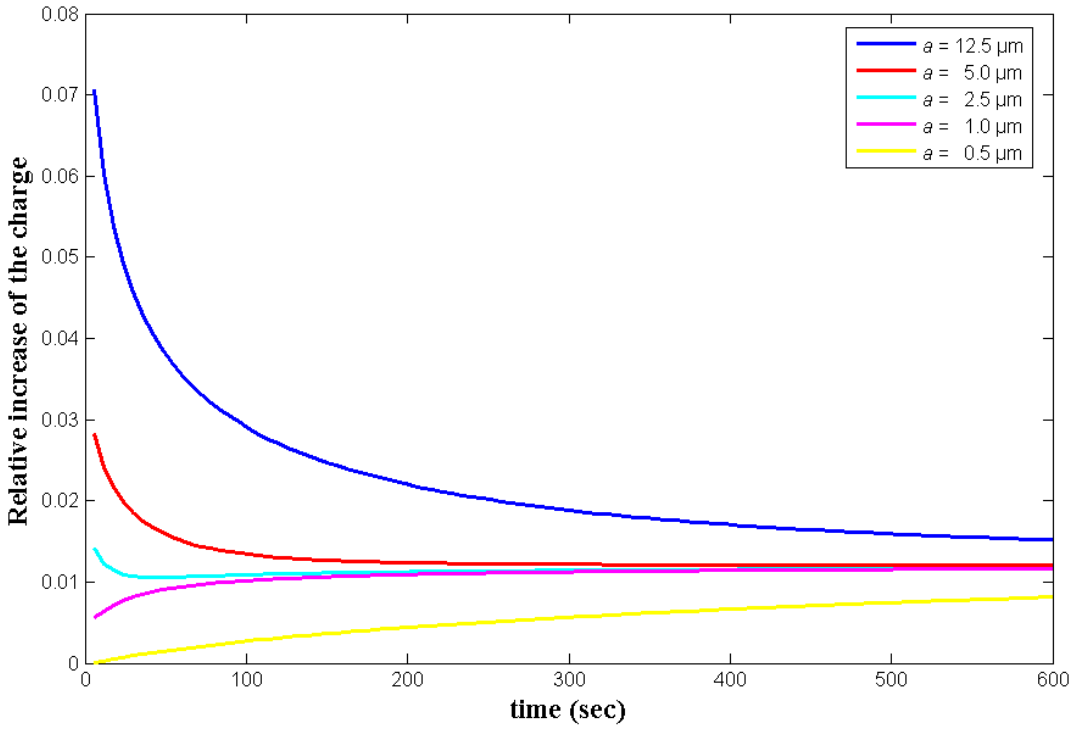

Figure 3-10. Relative increase of the charge deposited due to the transient current term, i.e. ($Q_{Model\ 2}$ - $Q_{Model\ 1}$)/ $Q_{Model\ 1}$, vs time, for different electrode disk radii *a*, from "Model 2" and under the conditions of "Data 2".

It shows that the effect of the transient current term on the total charge is limited (max 7% increase), and it seems to converge to values below 1.5% in all cases. The dependence on the size of the electrode is very clear, the influence of the transient current increasing significantly with an increase of the inlaid disc radius. Nevertheless, two different "regimes" seems remarkable, depending on the size of the electrode, with a transition occurring for a disc radius of about 2.5 µm. Above this value, the relative difference decreases with time, while below, it increases with time. This is due to the fact that in the case of a very fast volume growth, as is the case here for the smallest electrodes (see Figure 3-7), the transient current is first increasing, due to the growth of its surface area which superseeds its evanescent decay with time. Furthermore, it

raises faster than the steady-state term, since it is proportional to the area, while this latter varies with the square root of the area.

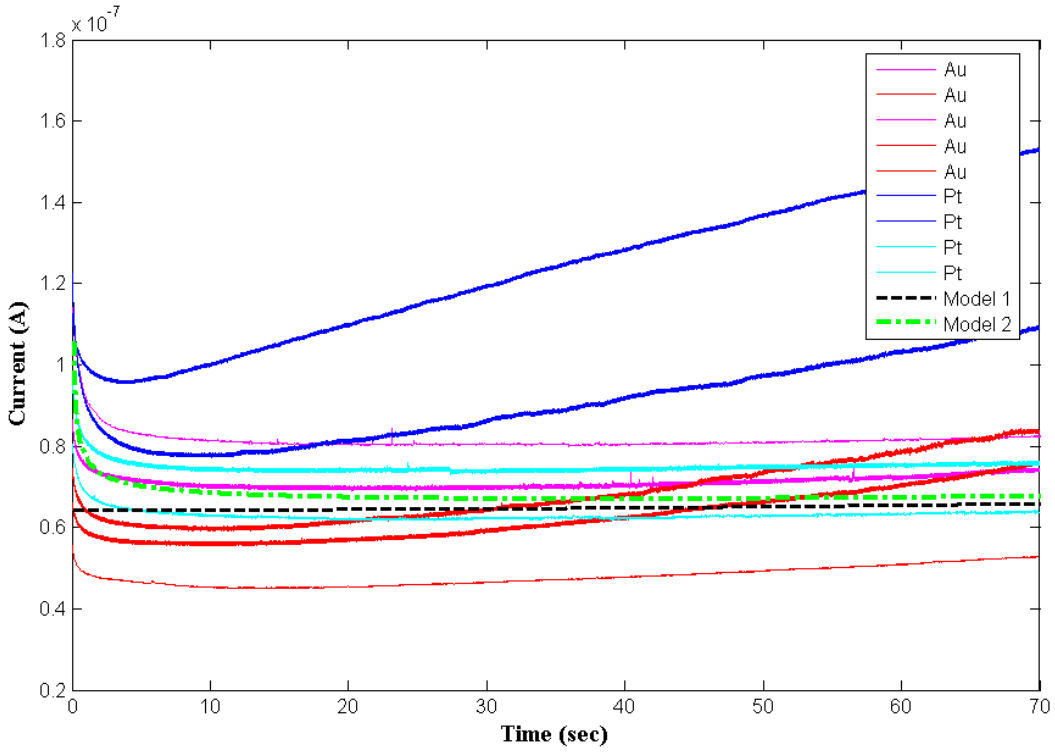

Figure 3-11. Plating current curves for disk radius of 12.5 µm : experimental data with gold (Au) or platinum (Pt) electrodes from "Data 2"; and theoretical matching computed from "Model 1" and "Model 2".

Analysis of the current plating curves (Figure 3-11) confirms that the transient current term does not influence significantly the total current magnitude and evolution rate at long times. Nevertheless, in the case of a low growth rate, its effect is non negligible. The modeling of the transient current seems consistent in view of the experimental curves, so we may conclude that, even though it improves the modeling, it is not the main reason for the discrepancy between theoretical and experimental charge data.

Concerning the plating current, our complete formulation, "Model 2", can still account for the evolution of only one of the two types of observed current responses. Furthermore, the experiments corresponding to the charge curves from "Data 1" with disc radii of 5 and 12.5 µm (two top curves in Figure 3-9) are more likely to stem from the second kind of evolution, a significant increase of the current during the early times, as this would explain the discrepancy between the theoretical models and the experimental data at long times in the charge curves. Therefore, it is clear that an intermittently appearing but frequent phenomenon, occurring at least during the early times, significantly increasing the current evolution rate, and strongly dependent on the electrode size is still not taken into account in our modeling.

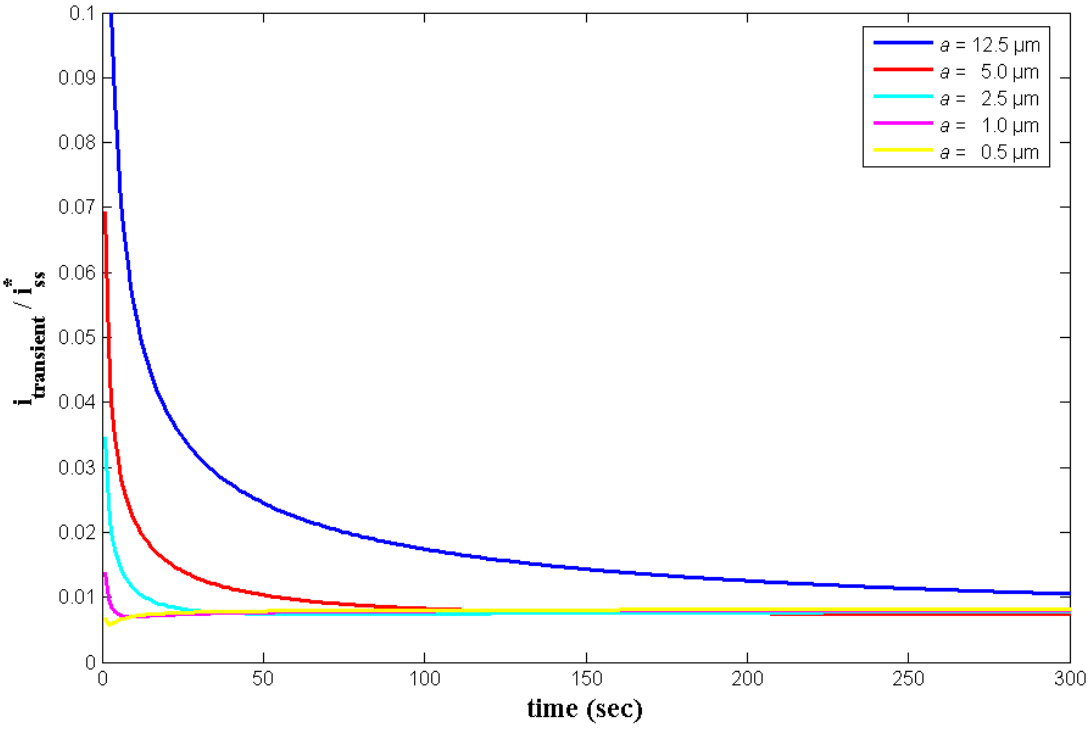

Figure 3-12. Ratio of the transient current, $i_{transient}$, to the quasi-steady-state current, i^*_{ss}, vs time, for different electrode disk radii *a*, from "Model 2" and under the conditions of "Data 2".

During the derivation of the current expression, we stated several times that the formula used, corresponding to fixed geometry, were accurate in our case, that of continuous growth of the electrode through deposition, only if the growth were much slower than the diffusion layer formation. This can be evaluated by considering the time for the total current to reach its quasi-steady-state value, or, in another words, for the transient term to fall under a given percentage of the steady-state one. The incorporation of the transient current in "Model 2" allows us to check the validity of the hypothesis. Figure 3-12 shows that the transient current is decreasing very fast, but that the time for it to become negligible is strongly dependent on the size of the electrode. From other analyses, we established that it does not vary much with the concentration c^b or the valence number n, but is very sensitive to a variation of the diffusion coefficient D_0. A higher D_0 and a smaller a significantly decrease the time to reach a quasi-steady-state. The time for the current to reach its steady state value within 5%, according to our modeling, is less than 1s for the three smallest electrodes, around 2s for the 5µm-radius one and about 12s for the largest one (12.5µm). These times, except for the last one, are negligible in view of the duration of the plating experiment, and a quasi-steady state will be reached quite quickly in all cases. Thus, we conclude that the quasi-steady state approximation is sufficiently accurate.

3.5 Conclusion: Refinement of the early-growth process required

From the comparison with the data, we can conclude that, under these experimental conditions (mainly listed in Table 3-1), our modeling is satisfactory for the disc electrodes of radius equal or smaller than 2.5µm. Nevertheless, we noted a significant discrepancy at long times in the charge curve between the theoretical and the experimental results. This discrepancy is likely to be engendered by a difference in the current increase rate at early times, which has

been noticed in about half of the data. We concluded from this analysis that a non-systematic but frequent phenomenon, occurring at least during the early plating times, significantly increasing the current evolution rate, and strongly dependent on the electrode size is not taken into account in our modeling.

Looking back at the assumptions made, there is one that has not been validated and which could have a significant effect on the current at the beginning of the process: the entire and instantaneous coverage of the inlaid disk by a single mercury film. Indeed, pictures from Mauzeroll, Hueske and Bard [8] (see Figure 4-6) show that, under experimental conditions almost identical to the ones of "Data 2", the penned configuration is reached only after several tens of seconds, and maybe even hundreds. Colyer, Luscombe and Oldham [13] also reported from optical investigations that during the early growth on a 12.5µm-radius disc-electrode, the amalgam does not present as a uniform layer but as isolated islands. In the case of separate droplets, the equilibrium shape assumed in our modeling, corresponding to a lowest surface area configuration, underestimates the interface area, and hence the plating current. So the assumption of instantaneous complete coverage is likely to explain the discrepancy between our model and the experimental data.

The early-growth is essentially composed of three processes, corresponding to successive but possibly overlapped periods: the nucleation, the growth of separate droplets on the conducting electrode disc, and their interaction that leads to coalescence. The first and third phenomena are the subjects of Chapter 4 and Chapter 5, respectively.

CHAPTER 4

NUCLEATION AND EARLY GROWTH

In this section, we analyze the nucleation and the early growth of a metal liquid phase through overpotential electrodeposition. Three points are of interest: the nucleation rate, the nuclei size and the number of nucleation sites. We begin by a theoretical review, based on the material of interest from the text of Budevski, Staikov and Lorenz [15], followed by a study of experimental data, and we end with the presentation and application of a nucleation plating current model.

4.1 Basics

The electrodepososition process includes three steps (see Figure 4-1). The first is the adsorption of the reduced ions on the surface, which is the process of the ions achieving an energetically stable position on the interface. These adsorbed atoms are called adatoms. The following step is the formation of a liquid phase by accumulation of adatoms. Precisely speaking, only this phenomenon is nucleation, but the term is often used loosely to include the related processes. In the nucleation process, the adatoms form a critical cluster, achieving a weakly stable state. The growth of the cluster is necessary for it to become a metal (Me) bulk phase, that is both homogeneous and stable.

The metal deposition on the surface and its stability, and thus the nucleation, are obviously strongly dependent on the redox reaction:

$$\mathrm{Me} \rightleftarrows \mathrm{Me}^{z+}_{solv} + z\mathrm{e}^{-} \tag{4.1}$$

Here, Me_{solv}^{z+} denotes the solvated metal ion, with z the valence number, and Me the corresponding metal molecule. The direction of the reaction is determined by the electrical potential, defined as the difference between the actual potential at the point considered in the solution, E, and the equilibrium redox potential of the reaction considered $E_{Me/Me^{z+}}$. This latter is given by the Nernst equilibrium:

$$E_{Me/Me^{z+}} = E^{o}_{Me/Me^{z+}} + \frac{RT}{zF}\ln\left(\frac{a_{Me^{z+}}}{a_{Me}}\right) \tag{4.2}$$

with $a_{Me^{z+}}$ and a_{Me} being the activities of solvated Me ions and Me bulk phase, respectively. $E^{o}_{Me/Me^{z+}}$ is the standard potential of the redox couple, established experimentally for standard conditions ($c_{Me^{z+}} = c_{Me}$ =1M, pressure=1 bar, temperature=25°C).

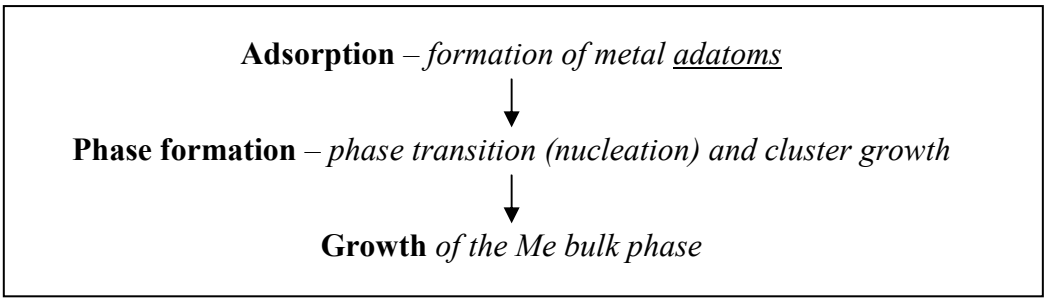

Figure 4-1. Electrodeposition process.

When the electrical potential is negative, it is called an overpotential (as opposed to an underpotential) for deposition (metal ion reduction):

$$\eta_c = E - E_{Me/Me^{z+}} < 0 \tag{4.3}$$

The larger the overpotential is, the faster the reduction goes, as the reaction speed, being an exponential function of the potential, is very sensitive to even a small deviation from the equilibrium.

Due to the occurrence of destabilizing energy fluctuations on the surface, the nucleation process requires some minimum overpotential for the critical clusters to become stable and grow. The likelihood of nucleation is often expressed as a function of the saturation, which is the difference between the actual electro-chemical potential and its value at the standard electrical potential:

$$\Delta\mu = \mu_{Me_{ads}} - \mu_{o,Me_{ads}} = -zF(E - E_{Me/Me^{z+}}) \tag{4.4}$$

where $\mu_{Me_{ads}}$ and $\mu_{o,Me_{ads}}$ are, respectively, the chemical potential of adatoms at $E \neq E_{Me/Me^{z+}}$ and $E = E_{Me/Me^{z+}}$. Consequently, according to the electro-chemical potential expression, the saturation is a function of the overpotential. Metal deposition, and therefore nucleation, takes place at overpotentials ($\eta_c < 0$), and thus at supersaturation: $\Delta\mu > 0$. It is important to note that while supersaturation is a necessary condition for nucleation, another parameter is essential to the process: the morphology of the surface, which sets the density and types of the nucleation sites.

4.2 Theory of nucleation

The theoretical work on nucleation has primarily focused on the explanation of three points of first interest: the different global deposition schemes, the original size of the nuclei, and the nucleation rate.

4.2.1) Deposition mechanisms – Growth modes

It is of first interest to understand the different ways the nucleation can progress, and especially, how will the first nuclei influence subsequent nucleation. Are the adatoms more likely to fix on an existing cluster, or will they continue to depose on the free surface till the electrode is totally covered ?

If the role of kinetics and of the metal-substrate (Me-S) alloy formation are neglected, then two parameters dominate the metal deposition mechanism: the binding energy, ψ, and the crystallographic misfit, characterized by the interatomic distances $d_{o,Me}$ and $d_{o,S}$ of the three dimensional metal and substrate bulk phases. In the case of a liquid metal phase formation, there is no crystallographic misfit issue, since the atoms are sufficiently free to adapt, but alloys are more likely to be formed, and some complicating factors such as inhomogeneous local diffusion and electric fields can be involved.

Generally, if $\psi_{Me_{ads}-Me} >> \psi_{Me_{ads}-S}$, the adsorbed Me molecules will fix preferentially on the Me phase, giving a three-dimensional growth by metal island formation. This mechanism is known as the "Volmer-Weber" growth mode. In contrast, if $\psi_{Me_{ads}-Me} << \psi_{Me_{ads}-S}$, the binding with the substrate molecules will be favored, inducing a layer by layer development of the deposit: this is the "Frank-van der Merwe" growth mode.

4.2.2) Nuclei size

Another point of interest in the study of nucleation is the critical size that a cluster needs to reach to become stable. This influences, for example, the size required for the nucleation sites, and hence their density.

The stability of a nucleus can be studied using the Gibbs energy of cluster formation, which represents the free energy change due to the metal deposition process. This quantity should be negative for spontaneous growth, and the lower it is, the more likely and rapid the process will be. The Gibbs energy of cluster formation is given by:

$$\Delta G(N) = -Nze|\eta| + \phi(N) \tag{4.5}$$

Both terms are functions of the size of the cluster (number of atoms *N*). The first one accounts for the energy gained by bringing *N* point charges (charge *ze*) from the reference state (of zero potential) to a surface with a favorable potential of magnitude $|\eta|$. The second term accounts for the energy necessary to create a surface between the phase of *N* Me molecules and the surrounding phases.

3-D nucleation

In the case of three dimensional "Volmer-Weber" nucleation, the second term of the Gibbs energy of cluster formation, i.e., ϕ in eq. (4.5), is approximately proportional to the area of the cluster surface: $\phi \propto N^{\frac{2}{3}}$. Figure 4-2 shows an example of possible behavior of the Gibbs energy of cluster formation as a function of *N*.

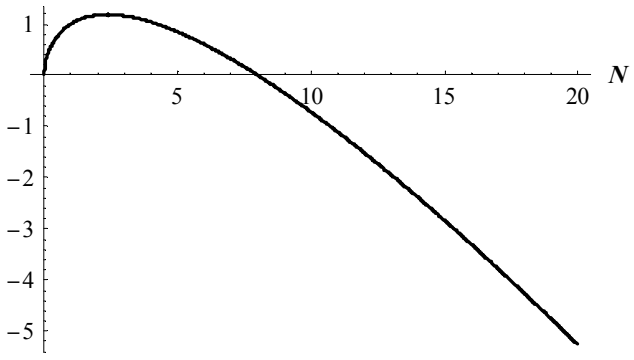

Figure 4-2. Example of a 3-D nucleation Gibbs energy-like function, $-c_1 N + c_2 N^{2/3}$ (c_1=1 and c_2=2).

As shown by the Figure 4-2, this model predicts the existence of a critical cluster size (here N_{crit}=3), that must be reached in order for the cluster to become stable. It further predicts a larger size (here N_{grow}= 8) to spur growth.

A more rigorous treatment of the surface energy term is obtained by writing $\phi(N) = A\,\sigma$, where σ is the average specific surface energy. The surface area A and cluster volume V are related by $A^3 = BV^2$ where B is a geometric parameter. The cluster volume is related to the number of Me molecules, $V=V_m N$, where V_m is the volume occupied by one molecule in the cluster. We can derive the growth cluster size N_{grow} by substituting the resulting expression for $\phi(N)$ into eq.(4.5) for the Gibbs energy ΔG and equating it to zero:

$$\Delta G_{grow}(N_{grow}) = -N_{grow} ze|\eta| + \sigma B^{\frac{1}{3}} \left(V_m N_{grow}\right)^{\frac{2}{3}} = 0 \tag{4.6}$$

which gives:

$$N_{grow} = \frac{BV_m^2\sigma^3}{(ze|\eta|)^3} \tag{4.7}$$

while the critical cluster size N_{crit} is obtained by equating to zero the derivative of ΔG with respect to the cluster size N:

$$\left(\frac{\partial}{\partial N}\Delta G\right)_{crit} = -ze|\eta| + \frac{2}{3}\frac{\sigma B^{\frac{1}{3}} V_m^{\frac{2}{3}}}{N_{crit}^{\frac{1}{3}}} = 0 \tag{4.8}$$

yielding:

$$N_{crit} = \frac{8BV_m^2\sigma^3}{27(ze|\eta|)^3} \tag{4.9}$$

The corresponding Gibbs free energy for the critical cluster formation, ΔG_{crit} , is:

$$\Delta G_{crit} = \frac{N_{crit} ze|\eta|}{2} \tag{4.10}$$

It is important to note that these expressions, because they use the continuum representation of surface energy, may lose validity for small N.

2-D nucleation

In the case of two-dimensional "Frank-van der Merwe" nucleation (layer deposition), the same parameters can be derived, based on $\phi(N) = P\varepsilon$, where P is the perimeter and ε is the average specific edge energy:

$$N_{crit} = \frac{b\Omega\varepsilon^2\sigma^3}{(ze|\eta|)^2} \tag{4.11}$$

where Ω is the area occupied by one atom. The perimeter is incorporated using $P^2 = 4bA$, with b a coefficient depending on the geometry. This gives:

$$\Delta G_{crit} = N_{crit} ze|\eta| \tag{4.12}$$

4.2.3) Nucleation rate

The rate of nucleation J is a function of the probability that thermal fluctuations will result in the formation of a critical cluster. It is given by the Volmer-Weber equation [15]:

$$J = K \exp\left(-\frac{\Delta G_{crit}}{kT}\right) \tag{4.13}$$

where k is the Boltzmann constant, and T is the absolute temperature. K is a coefficient that depends only slightly on overpotential, and can generally be treated as constant. But if we go further into details, it also depends on the attachment probability of one atom to the critical cluster, $w_{att,Ncrit}$, the density of nucleation sites, Z_o, and the geometrical form of the cluster, introduced by the Zeldovich factor Γ:

$$J = p\Gamma Z_o w_{att,N_{crit}} \exp\left(-\frac{\Delta G_{crit}}{kT}\right) \tag{4.14}$$

with p a constant. The Zeldovich factor Γ is a dimensionless number that is always less than unity, and usually is of the order of 10^{-2}. Through ΔG_{crit} and N_{crit} , it is a weak function of overpotential. For liquid droplets, it has the value:

$$\Gamma = \left(\frac{\Delta G_{crit}}{3\pi kTN_{crit}^2}\right)^{1/2} \tag{4.15}$$

For homogeneous surfaces, $Z_o \approx 1/\Omega$, where Ω is the surface occupied by one deposited atom. Thus Z_o is of the order of 10^{15} cm^{-2}. For inhomogeneous surfaces, Z_o is the number of active nucleation centers, which depends on configuration and overpotential.

Finally the attachment probability, $w_{att,Ncrit}$ depends on overpotential, but also on cluster form and the mechanism of attachment (direct transfer of ions from the solution and/or attachment of adatoms). In the first case it is proportional to the cathodic component of the exchange current density and so to $\exp[(1-\alpha)zF|\eta|/RT]$, and in the second to the adatom concentration and hence to $\exp[zF|\eta|/RT]$.

Although an understanding of the nucleation model contributes insight into the factors affecting the nucleation rate, the uncertainties on the parameters' values are too high to allow evaluation of the nucleation rate according to this model. Several other approaches have been developed to estimate the nucleation rate. We present the two most commonly used.

The classical approach

The "classical approach", considering the new phase as a continuum with bulk properties, is designed for macro-clusters. Using the models developed earlier for the critical energy of

cluster formation ΔG_{crit}, i.e., eqs. (4.9) with (4.10) or eqs. (4.11) with (4.12), and introducing them to Volmer-Weber equation, eq. (4.13), the predicted nucleation rate for a given temperature T is of the form:

$$J = B\exp\left(-\frac{C}{|\eta|^n}\right) \tag{4.16}$$

where B and C are constants, n=2 for a three dimensional nucleation and n=1 for a two-dimensional nucleation.

The classical approach, using bulk properties, is found to be useful primarily for small overpotentials, where the critical cluster size tends to be sufficiently large.

The atomistic model

The "atomistic model" has been derived to remedy to the failure of the classical theory for small clusters. Here, the excess energy function $\phi(N)$ defined in eq. (4.5) is expressed by the difference of the binding energies of N bulk atoms $N\phi_{kink,s}$ and the binding energies of the N atoms as arranged in the cluster $\sum_N \phi_{x^*,s}$, so that eq. (4.5) becomes:

$$\Delta G(N) = -Nze|\eta| + \left(N\phi_{kink,s} - \sum_N \phi_{x^*,s}\right) \tag{4.17}$$

The atomistic model uses the bond energies between the Me atoms themselves and those between the Me atoms and the substrate, assuming that the atomic interactions are confined to first nearest neighbors, to estimate $\sum_N \phi_{x^*,s}$. Only close-packed clusters are considered. The atomistic model is adequate for smaller clusters, and thus for higher overpotentials.

From the atomistic model, an expression for the nucleation rate of small clusters has been derived:

$$J = K_1(Z_o, N_{crit}) \exp\left(\frac{(N_{crit} + \beta^*) ze|\eta| - K_2}{kT} \right) \tag{4.18}$$

where β^* is a factor depending on the mechanism of attachment (usually 1 or 0.5), K_2 is a term accounting for the nucleus-substrate interaction and K_1 is a coefficient depending on Z_o and N_{crit}.

4.3 Direct experiments

From a practical point of view, we are primarily interested in determining, for mercury electrodeposition, whether the nucleation is instantaneous (all the possible sites are nucleated immediately and then the nuclei grow) or progressive (the sites are progressively nucleated and thus the first nuclei grow in parallel). The answer depends strongly on the overpotential.

Several techniques have been developed for the investigation of the nucleation rate [15]. Figure 4-4, reproduced from Ref. [15], shows the number of nuclei on a spherical platinum single crystal-electrode. The data was obtained by Toshev and Markov [29] by forming nuclei using an overpotential pulse of a given magnitude and duration, and then allowing the nuclei to grow until visible at a lower overvoltage. The density of nuclei, Z_{nuc}, was then determined by visually counting the developed droplets on a given surface area of the electrode.

Figure 4-4 shows that the steady state nucleation rate (J=dZ_{nuc}/dt) is attained after a short induction period. This corresponds to transient effects connected with the adjustment of the surface cluster population to the new overpotential conditions [15]. From an analysis of the experimental data, using the "classical" and "atomistic" models, Toshev and Markov [29] found that, in the overpotential interval of 84-106 mV, the nucleation energy ΔG_{crit} varies between 8.4 and 5.3×10^{-20} J, while the number of atoms forming the critical nucleus N_{crit} varies between 13 and 6.

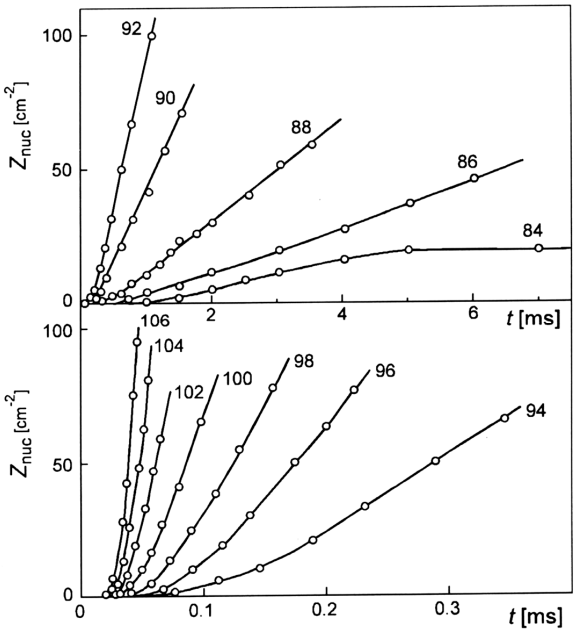

Figure 4-4. Experimental plots of the number of nuclei vs time in the electrodeposition of mercury on platinum at different overvoltages [mV].

"The time coordinate gives the length of the nucleation pulse in ms; its amplitude in mV is given by the numbers attached to the corresponding curves." Figure reproduced from Budevski et al. [15], itself based on the work from Toshev and Markov [29].

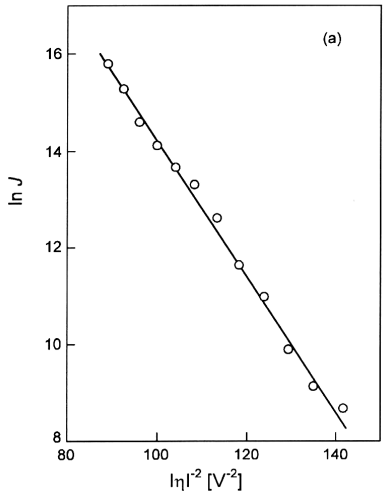

Figure 4-5. Log of the experimental steady-state nucleation rate values calculated from the data of Figure 4-4, vs the inverse of the overpotential to the square.

The most probable straight line is shown. Figure reproduced from Budevski et al. [15], itself based on the work from Milchev and Stoyanov [30].

The apparent linear relation between the log of the nucleation rate and the inverse of the square of the overpotential, presented in Figure 4-5, supports the validity of eq. (4.16) for three-dimensional nucleation, but the small number of atoms found (6 to 13 as stated above) discredits calculations based on bulk properties as in the classical approach. Nevertheless, if we extrapolate this relation to our values of interest (i.e., mercury deposition at a 0.7V overpotential): $\frac{1}{|\eta|^2} \approx \frac{1}{(0.7)^2} \approx 2$, we find $\ln(J) \approx 22$, which gives a nucleation rate J of the order of $10\ s^{-1}\ \mu m^{-2}$.

This has to be related to the density of nucleation sites, but this latter is difficult to estimate. The density of defects on a metal ranges from 10^{-3} to $10^{-1}\ \mu m^{-2}$ [12], but the density of nucleation sites is probably higher, since this gives between 0.025 and 2.5 sites on a disc of radius 5 µm. From the pictures of Mauzeroll, Hueske and Bard [8] (Figure 4-6), showing a platinum electrode surface at different times of a mercury plating experiment, the density of nuclei can be estimated to be at least 1 μm^{-2}.

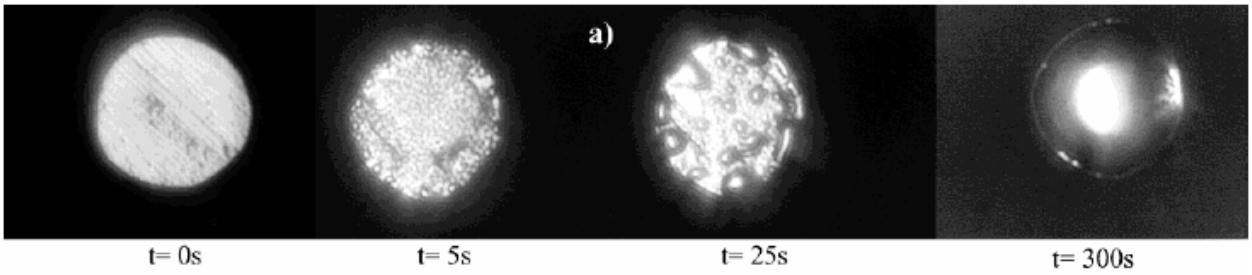

Figure 4-6. In situ micrographs of mercury deposition on a platinum 25-µm disc electrode.
Plating at -0.1 V vs Ag/AgCl, from a 10 mM $Hg^2(NO_3)_2$ solution with 0.1 M KNO_3 supporting electrolyte acidified to 0.5% with HNO_3. Figure reproduced from Mauzeroll, Hueske and Bard [8].

Based on these estimates of nucleation rates and nucleation site densities for the electrodeposition of mercury for amalgam electrode formation, it is reasonable to conclude that nucleation can be considered as instantaneous when modeling the process.

4.4 Plating current analysis

Another method developed to investigate the number of active sites and nucleation rate is the analysis of the plating current during the early transient response. Indeed, several models have been derived as attempts to express the plating current during a multiple nucleation and growth induced by a diffusion-controlled electrodeposition, and the issue is still being actively investigated [31]. The formulations, so far based mostly on theoretical considerations, are not yet satisfactory for the purpose of predicting the current density curve, and their goal is primarily to obtain a better understanding of the nucleation and early growth process. Nevertheless, the modeling is sufficient to give a general current density curve shape for the distinct cases of instantaneous and progressive nucleation, allowing one to characterize the regime by analyzing the plating current density curve in early times. Moreover, the study of the current maximum predicted in both cases allows one to estimate the number of nucleation sites and the nucleation rate (in the progressive case). Such an approach has been developed by Scharifker and Hills [32], and then attempted by many authors [31]. Several models are available, but they are mostly similar in the treatment of instantaneous nucleation, and the one of Scharifker and Hills, owing to its simplicity, is perhaps the most practical.

We do not present their derivation in detail in this thesis. Briefly, they consider hemispherical diffusion to a hemispherical nucleus, and re-express it as a 1-D diffusion to an equivalent area of plane surface, in order to reduce the problem dimensionality. The effect of the overlap of "diffusion zones" to individual nuclei is then treated statistically using Avrami's theorem [31],[33]. The resulting transient average current density, I'_{SH}, in the model of Scharifker and Hills, is [32]:

$$I'_{SH} = zFc^b \sqrt{\frac{D_0}{\pi \cdot t}} \left[1 - \exp\left(-\pi \cdot k \cdot N_0 \cdot D_0 \cdot t\right)\right] \tag{4.19}$$

with, for instantaneous nucleation:

$$k = \sqrt{8\pi \cdot \frac{c^b M}{\rho}} \tag{4.20}$$

Here, N_0 is the density of nucleation sites, z the valence of the mercury ions, F is the Faraday constant, D_0, c^b, and M are the diffusion coefficient of the mercury ions in the solution, their bulk concentration, and molar mass, respectively, ρ is the density of liquid mercury, and t is the time elapsed since the beginning of the potential step. Equation (4.20) gives the Cottrell current when N_0 goes to infinity (total coverage of the disk electrode by the nuclei), and predicts a lower current density for finite N_0. The physical basis for the reduced current density is the formation of a "diffusion zone" or area of lower concentration around an existing nucleus that prevents the formation of another one in the vicinity.

In this model, the maximum current density $I'_{SH,\max}$, and its corresponding time $t_{\max}$ are functions of the nucleation sites density N_0 [32]:

$$I'_{SH,max} \approx 0.6382 \cdot zFD_0 c^b \sqrt{kN_0} \tag{4.21}$$

$$t_{\max} \approx \frac{1.2564}{\pi \cdot k \cdot N_0 D_0} \tag{4.22}$$

Therefore, by determining the maximum current or its corresponding time, one can obtain the nucleation site density N_0 from experimental measurements.

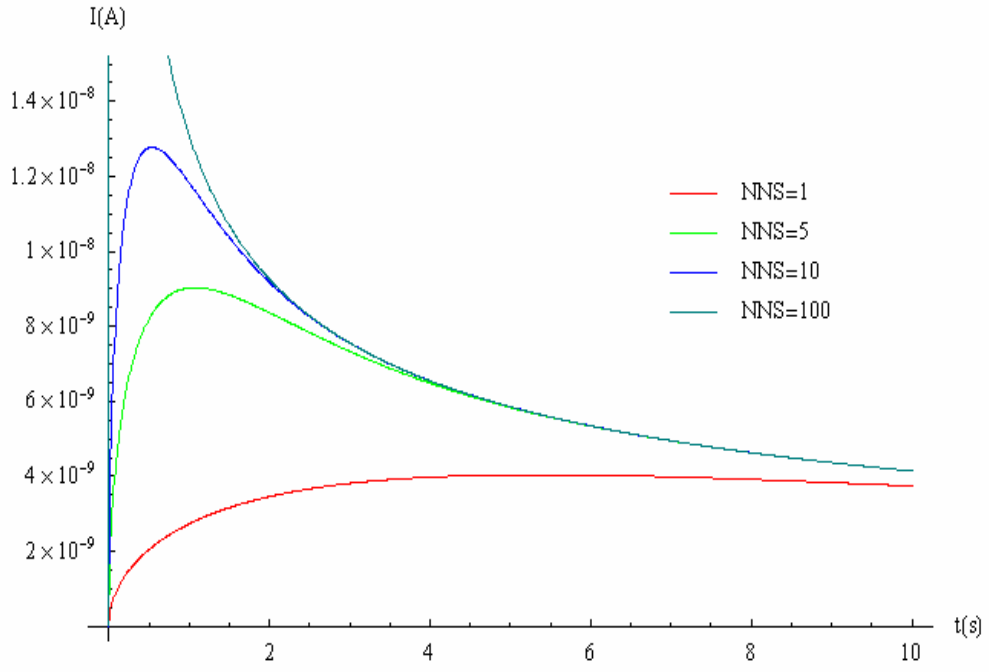

Figure 4-7. Example of transient currents computed with the Scharifker and Hills model, for different number of nucleation sites (NNS).

The parameters used are: a=12.5 µm, c^b=10 mM, D_0=6×10^{-10} m^2/s, z=2, corresponding to the experimental conditions of "Data 2" (see section 2.2).

Figure 4-7 has been plotted using eqs. (4.19) and (4.20). The total transient current is estimated using:

$$I' = \pi a^2 \cdot I_{SH} \tag{4.23}$$

and the nucleation site density is estimated using:

$$N_0 = \frac{NNS}{\pi a^2} \tag{4.24}$$

where *NNS* is the total number of nucleation sites. Equation (4.23) is an approximation of the total current, exact only in the limit of a uniformly accessible electrode (for which the current density is uniform on the disk electrode surface.) This approximation is reasonable for the disk interior, but less accurate at the edges where the current density is much higher. Nevertheless, the

effect of the number of nucleation sites on the predicted transient current response is interesting. From Figure 4-7, we see that the more nucleation sites there are for a given surface, the sooner and the higher the current maximum is. Such a maximum cannot be observed in our plating current data, "Data 2", which means, if the theory is right, that the current maximum occurs prior to the first measurement, which is at t=1ms. If we assume that the current maximum occurs at 1 ms, then, using eq.(4.22) and the parameters of Figure 4-7, we estimate a nuclei density N_0 of the order of 10 μm^{-2}. This is in good agreement with the nucleation sites density estimated in the previous section, but it implies a nucleation rate much faster than the one obtained earlier by extrapolation. Due to the inherent uncertainty of extrapolation, this observation does not invalidates the results. The estimates of nuclei density gives, from eqs.(4.21) and (4.23), a lower bound for the maximum current of about 3×10^{-7} A, which is fully compatible with the plating current data "Data 2" (see section 2.2), and thus supports the theory.

4.5 Conclusion

From the investigation of the nucleation process, we estimated that, for experimental conditions similar to the ones of our reference data, which are obtained with relatively high overpotential and mercury ion concentrations, the nucleation can be characterized as "instantaneous", and the density of nucleation sites is of the order of 10 μm^{-2}. Nevertheless, plating experiments at higher sampling rate are necessary to check the validity of the theory, and in this case to better estimate the number of nucleation sites. Another way to verify the model would be to dramatically decrease the concentration of mercury in the solution in order to effectively slower nucleation and growth and thus delay the current maximum.

Even if the investigations carried out in this chapter seem to all lead to similar conclusions and estimates, we have to mention possible alternative explanations and processes. Indeed, the high nuclei density exhibited in Figure 4-6, which constitutes our most explicit data, could be due to the presence of impurities on the electrode surface, and thus be not representative of the nucleation process on a clean electrode. Also, underpotential deposition experiments on gold and platinum [34, 35] show that the formation of a uniform amalgam layer may be energetically favoured, but the process time-scale would need to be investigated in order to know if this is relevant in our case of large overpotential deposition. A way to experimentally determine the impact of electrode surface contamination would be to proceed to multiple successive depositions, with removal of the deposit after each plating experiment. Mercury being a good solvent, the electrode would thus be cleaned by the successive electrodepositions, and comparison of the early depositions between the experiments would allow to verify the presence and influence of impurities on the electrode surface, and to analyse the deposition process on a clean electrode. Nevertheless, one would have to be careful since alloy formation could possibly alter the electrode surface at each experiment.

CHAPTER 5

DROPLETS INTERACTION: STUDY OF COALESCENCE

In this Chapter, the interaction between discrete droplets of the amalgam deposited on the electrode surface is investigated. The purpose is to determine whether some of the variability of plating current (especially on larger electrodes) can be explained by the likelihood of the occurrence of droplet coalescence. The hypothesis is that sometimes, the deposition may not result in a growing film or uniform penned sphere-cap, formed by the coalescence of the numerous nuclei, but instead result in the growth of separate islands of mercury that merge only after a certain time. An illustration of this phenomenon is provided in Figure 4-6. In order to be considered successful, our model must at least qualitatively predict the behavior observed in Figure 4-6: separate growth of adjacent droplets, which seem to remain stable until they reach a given size range, where they spontaneously coalesce.

In section 4-2 we investigate the ability to use a thermodynamic approach to predict coalescence. The approach is based on the classical DLVO theory [36, 37] [38] [39]. Finding that this approach cannot account for experimentally observed behavior, we turn in section 4-3 to an approach based on mechanical equilibrium using the concept of disjoining pressures [36]. Although our approach leaves considerable room for later refinement, it demonstrates success in predicting the behavior observed in real systems.

5.1 DLVO Theory of colloid stability

One of the most renowned [36, 37] models of charged surface interaction in an electrolyte is the DLVO (Derjaguin-Landau [38], Verwey-Overbeek [39]) theory of colloid stability. According to this model, the interaction between two identically charged surfaces in an electrolyte can be described quantitatively by an "energy of interaction", which is the sum of the energies due to Van der Waals attraction and electrostatic repulsion. Both of these contributions become appreciable when the surfaces are very close (within several nanometers).

The electrostatic repulsion is due to the interaction of the "double layers" induced by the similarly charged surfaces in the participating medium (see description of the phenomenon in Chapter 2). Thus, it depends mainly on the applied potential, the electrolyte type and ionic concentration, and the distance separating the two surfaces (see Figure 5-1). On the other hand, the Van der Waals attraction is an intermolecular phenomenon due to the correlation of electron fluctuations, or in other words due to induced dipolar interactions. Because it is more significant between dense aggregates of identical phase, the DLVO theory is able to neglect some aspects of the Van der Waals interaction between the droplets and the solution. Consequently, the main parameters of this phenomenon are the geometries of the neighboring surfaces, the separating distance, and the system considered (material of the droplets and separating medium). The electrostatic and Van der Waals forces are termed "long-range" interactions because they act over distances which are large on a molecular scale.

The DLVO theory does not take into account all interaction forces. Notably, it neglects the solvation, structural, and hydration forces, which may become dominant at very short distances (below 1 to 3 nm) [36]. The separation distance is a critical parameter also because it has to be large enough for the continuum approximation to hold. For an aqueous electrolyte with

a concentration of monovalent ions of 0.1M at 298K, the Debye length, which gives the order of magnitude of the electrostatic interaction distance, is about 1.3 nm [8],[12], which is at the lower bound of acceptable values [36]. Nevertheless, the DLVO theory seems able to quantitatively account for the stability of identically charged, similar in size and geometry mercury droplets in close contact in an electrolyte [40, 41]. By "close contact", we mean configuration where the two surfaces are separated by a distance of the scale of the long-range forces. Experiments have been carried out only for droplets of sizes of the order of the millimeter, but the theory predicts that the stability does not depend on this length scale, as we will see further. Another critical assumption is the absence of surfactants and of specific adsorption of anions, which could dramatically change the stability parameters. Finally, the model relies on perfect geometries. In our particular case, the failure of the model to account for the close presence of the conducting electrode surface is particularly noteworthy.

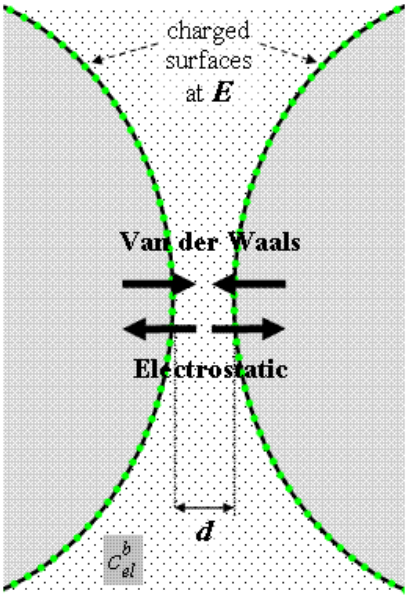

Figure 5-1. Schematic for DLVO theory.

5.2 Energy of interaction

The formulations of the interaction energies in the literature are quite similar, but some differences may be found in the electrostatic energy expression. We adopt Israelachvili's presentation of the DLVO model [36]. Two ideal geometries of interest are studied in the literature: the sphere, which can be used to describe the interaction of droplets growing without any constraints, and the infinite plane, which may describe the situation where two droplets are mutually locally deformed due to their growth while in close contact (see Figure 5-2).

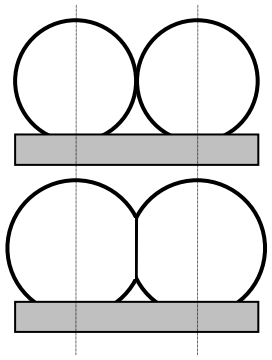

Figure 5-2. Illustration showing the evolution of the "contact" interface between two droplets. Initially, the droplets interact as spheres (top). If the droplets are confined, the interface could approach a planar configuration (bottom).

The electrode surface is shown here for illustration but not accounted for by the current theory.

From Figure 5-2, we notice that the available DLVO formulations, essentially based on interactions between spherical or plane surfaces, can not account for situation where the deposited droplets are subhemispherical (contact angle smaller than $\pi/2$).

For two bodies of the same material, whose areas of interaction can be approximated as two infinite planes, the Van der Waals attractive energy, per unit surface area, is given by [36]:

$$W_a^{"} = -\frac{A_H}{12\pi \cdot d^2} \tag{5.1}$$

where d is the distance separating the two planes, and A_H is the Hamaker constant, which depends upon the material of the bodies and the separating medium. To be strictly accurate, the Hamaker constant is not a constant but a function of interaction distance d, but the nature of the dependence is not well known [42]. The Hamaker constant for bodies of mercury separated by water is about 2×10^{-19} J [40, 42].

Determination of the electrostatic repulsive energy is more difficult, and an understanding of the results necessitates discussion of some critical assumptions. For two identically charged planes , a general formulation for the "electrostatic pressure", P_r, , is given by [36]:

$$P_r = kT\left[\rho_{el,m}(d) - \rho_{el,m}(\infty)\right] \tag{5.2}$$

where $\rho_{el,m}(d)$ and $\rho_{el,m}(\infty)$ are the total ionic concentration at the midplane (symmetry plane between the two droplets), for a finite separation distance d and an infinite one, respectively, k is the Boltzmann constant and T the temperature. P_r is a uniform pressure across the gap, and it is simply the excess osmotic pressure of the ions in the midplane over the bulk pressure. For a symmetric electrolyte at equilibrium, according to the Boltzmann distribution [36]:

$$\begin{aligned}\rho_{el,m}^{+}(d) &= \rho_{el}^{b}\exp\left(\frac{-(n_{el}e)\cdot\phi_m}{kT}\right)\\ \rho_{el,m}^{-}(d) &= \rho_{el}^{b}\exp\left(\frac{(n_{el}e)\cdot\phi_m}{kT}\right)\end{aligned} \tag{5.3}$$

where the superscripts "+" and "-" indicate the positive and negative ions, ρ_{el}^{b} is the ionic concentration of electrolyte ions in the bulk solution, ϕ_m is the midplane potential, e is the electron charge and n_{el} is the valence of the electrolyte. The potential requires a reference, which for this formulation is the electro-capillary maximum (ecm). The electro-capillary maximum is

the potential for which the measured surface tension of the interface between the body and solution will be greatest. This also corresponds to the potential which will not alter the ion concentrations from their bulk value. For mercury in an aqueous solution, the ecm is about −0.480 V vs NCE [17]. The bulk ion concentration ρ_{el}^{b} is related to the electrolyte bulk molar concentration, c_{el}^{b}, through:

$$\rho_{el}^{b} = c_{el}^{b} N_a \tag{5.4}$$

where N_a is the Avogadro number.

Recognizing that, at an infinite separation distance, the concentrations at the midplane are simply the bulk concentrations:

$$\rho_{el,m}^{+}(\infty) = \rho_{el,m}^{-}(\infty) = \rho_{el}^{b} \tag{5.5}$$

eq.(5.2) can be rewritten, for a 1:1 electrolyte, as:

$$\begin{aligned} P_r &= kT\rho_{el}^{b}\left[\exp\left(\frac{-(n_{el}e)\cdot\phi_m}{kT}\right)+\exp\left(\frac{(n_{el}e)\cdot\phi_m}{kT}\right)-2\right] \\ &= 2kT\rho_{el}^{b}\left[\cosh\left(\frac{(n_{el}e)\cdot\phi_m}{kT}\right)-1\right] \end{aligned} \tag{5.6}$$

Assuming that ϕ_m is small (within 50 mV vs ecm), which is a reasonable assumption when the midplane is at least one Debye length away from the droplet surfaces (i.e. $d \geq 2\lambda_D$) and the applied potential is low (within 0.1V vs ecm), then eq. (5.6) can be approximated by:

$$P_r \approx \frac{(n_{el}e)^2\cdot\phi_m^2\cdot\rho_{el}^{b}}{kT} \tag{5.7}$$

Considering eqs.(5.3) or (5.7), determination of P_r is seen to require finding the midplane potential ϕ_m. Under the earlier assumptions of small potentials and large separation, the weak overlap approximation can be used to estimate ϕ_m [36]. In the weak overlap approximation, ϕ_m

is simply approximated as the sum of the potentials from each surface at a distance *d*/2, as derived for the case of one surface alone. The result is [36]:

$$\phi_m \approx \frac{8kT\chi}{n_{el}e}\exp\left(-\frac{d}{2\lambda_D}\right) \tag{5.8}$$

where λ_D is the Debye length, and χ is a non-dimensional coefficient accounting for the influence of the applied wall potential (vs ecm), $E_{/ecm}$ [36]:

$$\chi = \frac{\exp\left(n_{el}eE_{/ecm}/(2kT)\right)-1}{\exp\left(n_{el}eE_{/ecm}/(2kT)\right)+1} \tag{5.9}$$

From eq.(5.9) we find that $\chi = 0$ when $E_{/ecm}$=0, and $\chi = 1$ when $E_{/ecm} = \infty$. The Debye length can be expressed by [36]:

$$\lambda_D = \sqrt{\frac{\varepsilon\varepsilon_0 kT}{\rho_{el}^b (n_{el}e)^2}} \tag{5.10}$$

where $\varepsilon\varepsilon_0$ is the dielectric permittivity of dilute aqueous solution, $\varepsilon\varepsilon_0 = 6.95\times10^{-10}$ $C^2/N/m^2$.

Introducing eq.(5.8) into eq.(5.7), we obtain an expression for the electrostatic pressure:

$$P_r = 64kT\rho_{el}^b\chi^2\exp\left(-\frac{d}{\lambda_D}\right) \tag{5.11}$$

The electrostatic repulsive energy, per unit surface area, is derived by integration with respect to *d*, between an infinite separating distance, where the interaction energy vanishes, and a finite separation distance *d* [36]:

$$W_r^{"} = 64kT\rho_{el}^b\chi^2\lambda_D\exp\left(-\frac{d}{\lambda_D}\right) \tag{5.12}$$

The corresponding relations, for the interaction energies in the case where the interface is constituted by two symmetrical sphere surfaces, are derived from the planar formulations using

the Derjaguin approximation [36]. The Derjaguin approximation gives, in the case where the interaction range and the separation distance are much less than the radii of the spheres, i.e. when the interaction is limited to the portion of the spheres surfaces that are in close proximity, a relation between the force law $F_{sphere}(d)$ between two spheres and the energy per unit area $W''_{plane}(d)$ of two flat surfaces:

$$F_{sphere}(d) \approx 2\pi \left(\frac{R_1 R_2}{R_1 + R_2} \right) \cdot W''_{plane}(d) \tag{5.13}$$

where R_1 and R_2 are the respective radii of the two spheres. The range of the interaction being of a few nanometers, as discussed earlier, this relation holds when the droplets are not smaller than about 0.1 μm. The force is then integrated with respect to d to give the interaction energy in the sphere case.

The Van der Waals attractive energy between two spheres of equal radius, calculated using the Derjaguin approximation, eq.(5.13), is:

$$W_a = -\frac{A_H R}{12 d} \tag{5.14}$$

where R is the radius. The electrostatic repulsive energy for identically charged spheres is:

$$W_r = 64\pi R k T \rho_{el}^{b} \chi^2 \lambda_D^2 exp\left(-\frac{d}{\lambda_D} \right) \tag{5.15}$$

Consideration of eqs.(5.14) and (5.15) shows that, for equally charged spheres of equal radius R, both interaction energies are proportional to R.

The total interaction energy W, or energy per unit area W'', is obtained by summing the respective contribution of the Van der Waals and electrostatic energies. Plots of the total interaction energy as a function of distance d are presented in Figures 5-3 and 5-4. In these and

all other calculations in this Chapter, the parameters given in Table 5-1 are used, unless specifically stated otherwise. The values in Table 5-1 correspond to those of the reference case presented in Chapter 2, except for the applied potential. The potential used is closer to the ecm, due to the assumptions of small potential in the DLVO theory derivation. Some extension of the results to more practical potential is possible by observing that a larger potential will always inhibit coalescence.

Table 5-1. Reference parameters used in numerical analysis.

Parameter	Symbol	Value
Hamaker constant	A_H	2×10^{-19} J
Applied potential vs ecm (=$E_{/SCE}$+0.48V)	$E_{/ecm}$	0.1 V
Bulk concentration of electrolyte	c_{el}^{b}	0.1 M
Valence of electrolyte ions	n	1
Temperature	T	298 K
Permittivity of water	$\varepsilon\varepsilon_0$	6.95×10^{-10} $C^2/N/m^2$

Figures 5-3 and 5-4 indicate that in our case, an energy barrier, i.e. a positive interaction energy peak, is present. This means that based on thermodynamic considerations from the DLVO theory, and if no other energy is involved, two neighboring droplets will repel one another. According to the plots, they will achieve a stable spacing with a separation distance of about 4 Debye lengths (5nm). The maximum interaction energy occurs, as expected, at a separation distance of about one Debye length for the planes, and a bit less for the spheres. If this energy barrier is overcome, the coalescence will then be spontaneous due to the dramatic drop in interaction energy through negative values, which represents a strong attraction. The equations describing the interaction energy have shown that two parameters, having opposite influences,

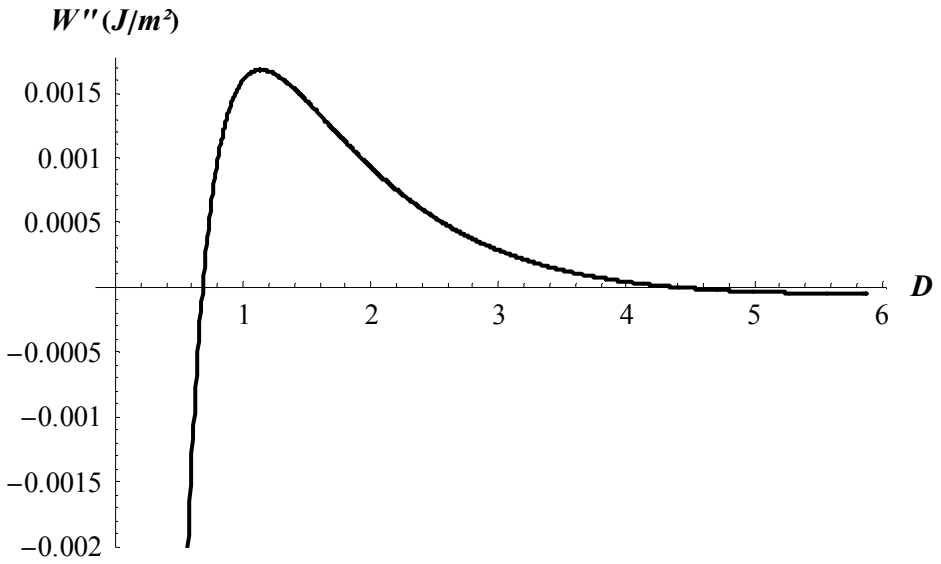

Figure 5-3. Interaction energy per unit area, W'', as a function of non-dimensional separation distance, $D = d/\lambda_D$, for two identically charged thick planes of mercury separated by water.

The numerical values used are listed in Table 5-1.

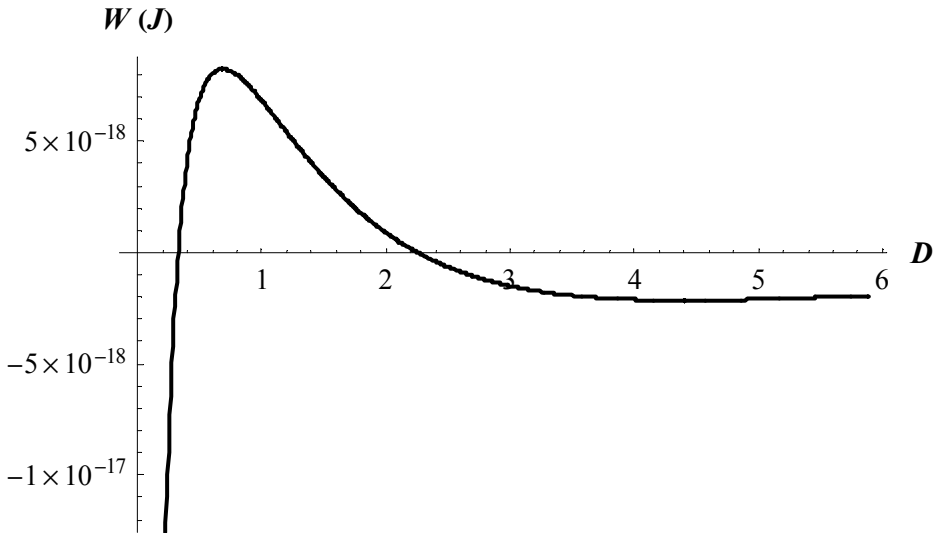

Figure 5-4. Interaction energy, W, as a function of non-dimensional separation distance, $D = d/\lambda_D$, for identically charged mercury spheres of radii 1μm separated by water.

The numerical values used are listed in Table 5-1.

determine the energy barrier: the Hamaker constant and the potential. An increase of the former lowers the energy barrier, as does a decrease of the latter. In our example case, the barrier vanishes for a ten times higher A_H or a potential within 0.1V of the ecm, resulting in a prediction of spontaneous coalescence. The electrolyte concentration has little effect on the energy barrier value, but it significantly changes the corresponding distance.

5.2.1) Stability regime maps

The Hamaker constant is a fixed parameter for a given system, as it is determined by the droplet material and the solution. Therefore, it is interesting to know, depending on the concentration of the electrolyte, what is the critical potential, i.e. the electrical potential E_{crit} so that the interaction energy maximum vanishes. For a higher E, there is an energy barrier, so a repulsion, whereas none will occur for a lower E, leading to a spontaneous coalescence. Thus, a plot of E_{crit} versus c_{el}^{b} constitutes a regime map, giving the stability of the droplets in close contact based on the experimental parameters [40, 41]. This relationship is obtained by finding the combination of E and c_{el}^{b} for which the interaction energy maximum has a value of zero:

$$\begin{cases} W(E_{crit}, c_{el}^{b}) = 0 \\ \dfrac{\partial W}{\partial d}(E_{crit}, c_{el}^{b}) = 0 \end{cases} \tag{5.16}$$

Equation (5.16) gives that the separation distance for the interaction energy maximum, d_{crit}, for the case of critical potential separation distance, is the Debye length, λ_D , for two spheres and twice the Debye length, $2\lambda_D$, for interacting the planes. Further, eq.(5.16) is used to obtain the critical potential, E_{crit} , as a function of the electrolyte concentration, c_{el}^{b}, plotted in Figure 5-5. It is interesting that for the case of spheres of equal radii, R, the curve is independent of R.

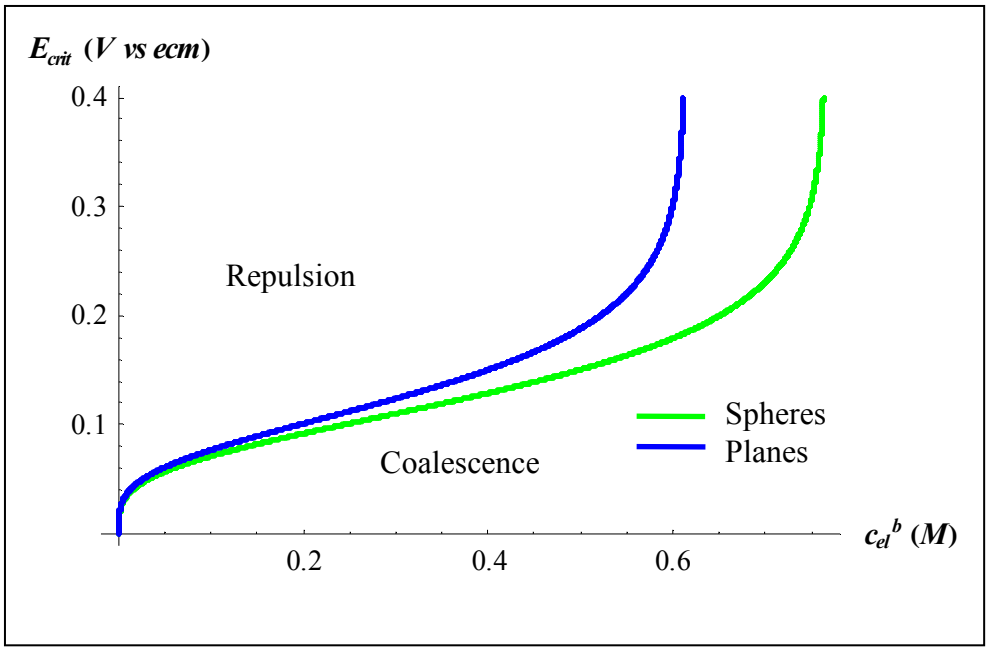

Figure 5-5. Regime map giving the stability of two identically charged mercury droplets in water, in the sphere and plane case, depending on the applied potential *E* and the bulk electrolyte concentration c_{el}^{b}.

For the sphere case, the curve does not depend upon the droplet radii, *R*. The numerical values used are listed in Table 5-1.

Figure 5-5 shows the existence of a critical concentration, above which coalescence is spontaneous for any value of the potential. The basis of these results on an assumption of low potential, described earlier, could draw this conclusion into question; however, similar curves have been established by experiments [40, 41]. The explanation for this phenomenon is that high concentration solutions have thin double layers, and thus the electrostatic repulsion range is small. Because the Van der Waals attraction soars as the separation distance vanishes, it dominates over the electrostatic repulsion at the extremely small distances, leading to spontaneous coalescence. Figure 5-5 also shows that a sufficiently small voltage allows an immediate merging, for any value of the electrolyte concentration. The reference case (parameters in Table 5-1), lies in the bottom-left part of the map (E=0.1V vs ecm and c_{el}^{b} =0.1M),

near the edge of the region for which repulsion is predicted. Also, according to the map, the same if we consider the typical plating potential value (E = 0.1V vs Ag/AgCl = 0.38 vs ecm) plating conditions fall in the top left corner, far into the repulsion zone. By a parametric analysis, the stability map was found to be sensitive to the valency of the electrolyte and the Hamaker constant, but not to such an extent as to change the stability prediction for the latter case.

The DLVO analysis predicts repulsion for experimental regimes of interest, and shows no dependence of this on the droplet size. We conclude that DLVO theory can account for the non-coalescence of mercury droplets under usual experimental conditions, and this conclusion has been reached by similar analyses and experiments [40, 41]. We must next find an explanation for the eventual merging of the droplets, that can be seen on Figure 4-6, and an analyzis of the influence of the conducting surface of the electrode is still necessary.

5.2.2) Potential of coalescence

The DLVO model seems to provide a good understanding of why the droplets do not coalesce directly, but we need then to find the mechanism that will finally overcome the repulsion and lead to coalescence. A natural idea is to compare the energy barrier from the DLVO model with a "potential of coalescence", defined as the energy that would be released by the merging of two droplets, due to the reduction in surface energy. The case considered here treats two droplets of equal size laying on a non-participating surface, assuming a constant contact angle α.

The potential of coalescence, U_{coal}, is defined by subtracting the total interfacial energy of the two configurations depicted in Figure 5-6:

$$U_{coal} = \gamma_{drop/sol}(A - A') + \gamma_{drop/met}(A_s - A_s') \tag{5.17}$$

where $\gamma_{drop/sol}$ and $\gamma_{drop/met}$ are, respectively, the interfacial energies per unit area between the droplet material and the solution, and between the droplet material and the electrode metal; A, A', and A_s, A_s', are the corresponding interface areas of the system before and after coalescence, respectively. The interfacial energy between mercury and an aqueous solution is around 0.36 J/m^2 [17]. The interfacial energy between mercury and a metal is not well known, but it can be estimated of the order of 2 J/m^2 (average value for a metal-liquid contact [36]).

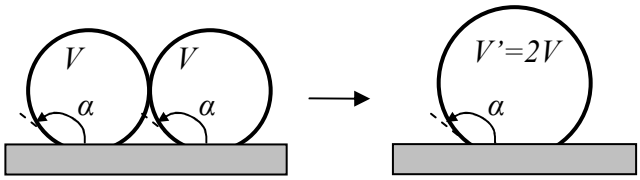

Figure 5-6. Schematic showing the change in total surface area of the system induced by the merging of two droplets of equal size, at constant contact angle α, used in defining the "potential of coalescence".

The electrode surface is accounted for the geometry of the droplet, but neglected in droplets interactions considerations.

The following derivations correspond to the case where droplets are hemispheres ($\alpha=\pi/2$), chosen in order to get simple formulations. The volume of a hemisphere is related to its curved surface area by:

$$V^2 = \frac{A^3}{18\pi} \tag{5.18}$$

and to its base surface area by:

$$V^2 = \frac{4 A_s^3}{9\pi} \tag{5.19}$$

Introducing eq.(5.18) and (5.19) into eq.(5.17) with $V'=2V$ yields, after factorization:

$$U_{coal} = \left[\gamma_{drop/sol} \left(2\right)^{1/3} + \gamma_{drop/met} \left(\frac{1}{4}\right)^{1/3} \right] \cdot \left(9\pi V^2\right)^{1/3} \cdot \left(2 - 2^{2/3}\right) \tag{5.20}$$

Next, expressing the volume of a hemisphere as a function of its radius R and simplifying, we obtain an expression for the "potential of coalescence" in the hemisphere case, as a function of droplet radius:

$$U_{coal} = \left[2\gamma_{drop/sol} + \gamma_{drop/met} \right] \cdot \pi R^2 \cdot \left(2 - 2^{2/3}\right) \tag{5.21}$$

Defined this way, the "potential of coalescence" is directly proportional to R^2. To compare the potential of coalescence to the total interaction energy for two hemispheres, we calculate their ratio, using eqs.(5.14), (5.15) and (5.21):

$$\frac{U_{coal,h}}{W_h} = \frac{U_{coal}}{2\left(W_a + W_r\right)} = \frac{\left[2\gamma_{drop/sol} + \gamma_{drop/met} \right] \pi \left(2 - 2^{2/3}\right)}{-\frac{A_H}{12d} + 64\pi kT \rho_{el}^b \chi^2 \lambda_D^2 \exp\left(-\frac{d}{\lambda_D}\right)} \cdot R \tag{5.22}$$

where h stands for the hemispheres case. Evaluation of eq.(5.22) for d corresponding to the separation at the energy barrier maximum for the reference case (parameters of Table 5-1), yields a ratio of the order of $\left(10^{11} m^{-1}\right) R$. Thus the two energies would balance for hemispheres with radii of around $0.01\,\text{nm}$, a size smaller than one molecule, so a scale for which the continuum assumption does not hold. For droplets of size of the order of 1μm, the "potential of coalescence" is five orders of magnitude greater than the energy barrier, and our thermodynamic considerations would then predicts a spontaneous coalescence. This result does not explain the experimental observations in Figure 4-6, which correspond to our reference case (Table 5-1) with a higher potential, but does not constitute a clear contradiction, since as stated earlier, a higher potential is expected to prevent more the coalescence. Nevertheless, we draw the conclusion that

the "potential of coalescence model" fails to predict the transition from adjacent growth to coalescence for spherical interactions.

The possibility still exists that this method of analysis could be correct, if the local interaction energy is better described using the model for infinite planes. Hence, we consider the configuration illustrated in Figure 5-2, where two droplets are constrained to grow next to each other, and develop a planar "contact" interface. From Figure 5-3 one can estimate the energy barrier as:

$$W_{\max} \approx 1.5 \times 10^{-3} A_c \tag{5.23}$$

where A_c is the contact area. The contact area will be at most of the order of R^2, and the resulting ratio of the potential of coalescence to the energy barrier is: $U_{coal}/W \approx 10^3$. Thus, this model would also predict an instantaneous coalescence for two hemispheres in our reference case. Furthermore, it exhibits no size dependence, as expected to account for the fact that most droplets are in the same size range before coalescing on the observations presented in Figure 4-6. Consequently, this modification has failed to correct the predictions of the model.

5.3 Disjoining pressure

The energy approach, based on DLVO theory has not given a satisfactory explanation for the mechanism leading to coalescence. Therefore, we consider another approach based on mechanical equilibrium. This approach does not contradict the thermodynamic energy approach, but instead includes the possibility of metastable states. The implication is that systems in metastable states of mechanical (but not energetic) equilibrium, should eventually proceed to thermodynamically preferred, stable, equilibrium states. However, it may be that this procession occurs only on a very large time scale.

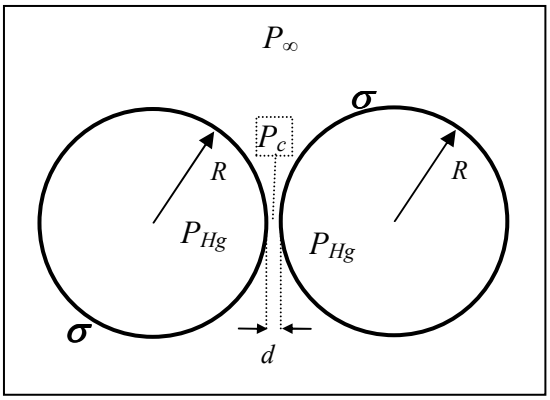

Figure 5-7. Illustration for the determination of mechanical equilibrium between two droplets in a solution.

The idea is to study the consequence of a mechanical equilibrium at the interface between two identical droplets (see Figure 5-7). The pressure difference across the droplet/solution interface, away from the interaction zone, is given by the Young-Laplace equation:

$$P_{Hg} - P_\infty = \frac{2\sigma}{R} \tag{5.24}$$

where P_∞ is the rest pressure in the bulk solution, P_{Hg} is the pressure inside the mercury droplet, R is the droplet radius and σ is the surface tension of mercury in aqueous solution. At mechanical equilibrium, the pressure is uniform inside the mercury droplets, and also outside in the solution. Hence:

$$P_c = P_\infty \tag{5.25}$$

where P_c is the pressure at the "contact" point, i.e. the point where the droplets' surfaces are the closest. Consequently, using eq.(5.24), mechanical equilibrium requires that:

$$P_{Hg} - P_c = \frac{2\sigma}{R} \tag{5.26}$$

The pressure difference across the mercury/solution interface at the contact point is called the disjoining pressure, Π. Its value can be predicted using DLVO theory:

$$\Pi = P_{Hg} - P_c = P_r - P_a \tag{5.27}$$

where P_a is due to the Van der Waals attraction and P_r is due to electrostatic repulsion. Using eqs.(5.26) and (5.27) the statement of mechanical equilibrium becomes:

$$\frac{2\sigma}{R} = P_r - P_a \tag{5.28}$$

Equation (5.28) can be considered a requirement that, at mechanical equilibrium, the forces exerted on the solution due to the droplet/solution interface must be the same, both at the contact point and far from the contact point. Far from the contact point, the forces are accounted for by the surface tension. Close to the contact point, a more detailed accounting of electrostatic and Van der Waals interaction is required; it is for this accounting that the concept of disjoining pressure is incorporated.

The electrostatic repulsion component of the disjoining pressure, P_r, has been discussed in section 4.2, and eq.(5.11) gives an expression for its calculation in the case of the interaction between identically charged planes. We use a planar model as an approximation of the interaction zone, and the appropriate expression for P_r is repeated here:

$$P_r = 64kT\rho_{el}^{b}\chi^2 \exp\left(-\frac{d}{\lambda_D}\right) \tag{5.11}$$

It is worth emphasizing again that eq. (5.11) requires assumptions of sufficient separation and small potential.

The attractive component of the disjoining pressure, P_a, , is calculated as the derivative with respect to separation distance of the energy of interaction (per unit area) due to Van der Waals forces, i.e. eq (5.1), which gives:

$$P_a = \frac{A_H}{6\pi d^3} \tag{5.29}$$

With eqs. (5.29) and (5.11), the criterion of mechanical stability , eq. (5.28) becomes a functional relationship between R and d. The solution to eq.(5.28) is plotted in Figure 5-8 for the values of the parameters listed in Table 5-1. The area of negative radius has been stripped since it has no physical meaning. The top-left corner of the diagram corresponds to a situation where mechanical and energetic considerations (see Figure 5-3) predict coalescence, due to the fact that the Van der Waals attraction overcome the electrostatic repulsion when the two surfaces get so close. Thus, droplets can not exist in this configuration according to our model, they would have coalesced when entering the zone. The "stable" zone corresponds to situations where the pressure exerted on the droplet surface due to its curvature is higher than the disjoining pressure. Consequently, the surface can keep its regular shape while the droplet grow and get closer to its neighbor. On the regime separation line, the pressure on the droplet surface due to surface tension is balanced locally by the interaction pressure: the droplets can not grow further keeping their optimum shape. They will then develop an increasing interface (as illustrated in Figure 5-2) while remaining at the same distance, becoming "unstable" since a physical or electrostatic fluctuation would be more and more likely to prompt their coalescence. Thus, it is difficult to predict exactly when the merger will happen, but the model tells us that the probability it does, proportional to the droplet-droplet interface area, increases with time through the droplets growth.

As explained above, Figure 5-8 presents a stability regime map for two mercury droplets in "close contact" in water, depending on their size and the separation distance. It shows that for relevant separation distances (d between 1 and a few Debye lengths), we find stable sizes in the expected range (from zero to few μm). Logically, as d increases, the interaction between the two spheres decreases, allowing them to remain stable at larger sizes. This map suggests that droplets

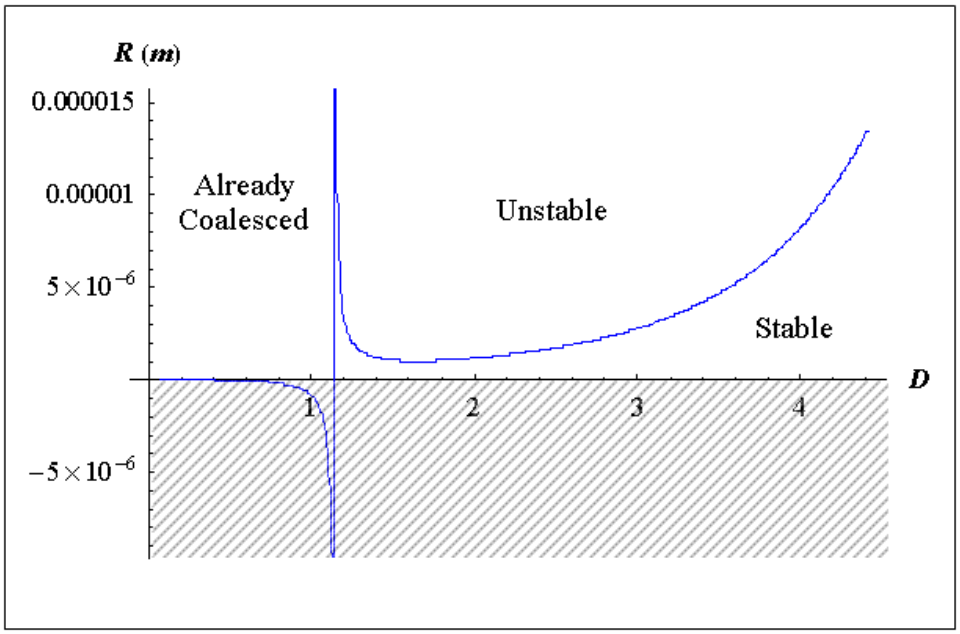

Figure 5-8. Regime map giving the stability of two identically charged mercury droplets in "close contact" in water, according to the disjoining pressure approach, as a function of droplets radius *R* and non-dimensional separation distance, $D = d/\lambda_D$.

The numerical values used are listed in Table 5-1.

below a critical size (about 1μm) are stable to very close approach, but, as their size increases, they will transition to the unstable regime and then coalesce. Thus, this model predicts the behavior observed in Figure 4-6. This approach seems to explain why all the separated droplets are roughly of the same size, before they finally coalesce. Indeed, the density of nuclei estimated in Chapter 4 does not allow a droplet to grow significantly before getting in "contact" with a neighbor. Then, this configuration remains stable until the droplets reached the critical size. The ability of this model to quantitatively describe our problem still needs to be confirmed. For example, we expect that larger potentials (vs ecm) will inhibit coalescence, but we should develop a method to quantify this effect. Importantly, the influence of the conducting surface has not been studied yet.

5.4 Conclusion

The analysis of droplet interactions via the DLVO theory has led to a possible explanation of coalescence, and the ability to quantitatively predict the process. The energetic approach to the problem provided an understanding of the forces involved and the relevant parameters, but failed to provide an explanation for the observed apparent initial repulsion of the surfaces, followed eventually by merging of the droplets. Nevertheless, the derivation of an interaction regime map, based on the applied potential and the ionic concentration, revealed two interesting limiting regimes. These regimes should allow experimental verification of the applicability of the DLVO theory in the particular case of mercury electrodeposition on a metal electrode. The first regime predicts vanishing of the repulsion force when the applied potential is brought near the electro-capillary maximum. The second regime predicts the existence of an ionic concentration, above which the coalescence is also spontaneous, for any potential. These two regimes should be quite easily accessible by experiment, and one could hope to see the influence of the spontaneous coalescence in the plating current curves.

An approach using the concept of the disjoining pressure and based on a requirement of mechanical equilibrium was the last development. This approach produced a regime map for the stability of two droplets which qualitatively agrees with experimental observations. A critical size, required to be reached for the coalescence to become probable, was found of the order of one to a few micrometers. In spite of this initial success, we identified the need for much development. This includes the development of formulations for potentials not in the vicinity of the electro-capillary maximum. Furthermore, the influence of the conducting surface as not been carefully studied yet. Upon initial consideration we believe the effect of the conducting surface

will be to inhibit coalescence, due to an increase of the osmotic pressure on the surface induced by the addition of its "double-layer" to those of the droplets.

To be complete, we have to mention here another possible explanation for the droplet delayed coalescence. A flow between the two droplets, through induced lubrification forces, could prevent or delay their coalescence [43]. Such a flow could result from two different phenomena: the relative motion of the two surfaces involved, or a temperature gradient along the droplets surface. Indeed, this would induce a curvature gradient by thermocapillary effect, leading to advection over the droplet surface. In the second chapter, when we presented the electrodeposition process, we assumed that it was isothermal, but this has not been verified.

CHAPTER 6

CONCLUSION

The electrodeposition of mercury onto a metal electrode is a common experiment in electrochemistry, used to enhance the electrode capabilities. Recent applications, especially in scanning electrochemical microscopy (SECM), have developed an interest in the miniaturization of this kind of electrode. The scale has fallen to the micrometer, and smaller sizes are already being considered. The electrodeposition of the mercury seemed, from the theoretical point of view, rather straightforward. But a lack of reproducibility of the plating data and eventually some direct observations have revealed that, at the microscopic scale, the theory fails to predict, with reliability and accuracy, the electrode mercury-coating process. This has prompted an interest in the refinement of the modeling of mercury electrodeposition process. First, global and semi-empirical models have been developed, which proved to be accurate enough in particular cases, but a deeper understanding of the actual processes involved is needed, and thus the modeling refinement effort joins a larger investigation on electrochemical processes at the micrometer and smaller scales. The study presented here is an attempt to reinvestigate the mercury electrodeposition theory for microelectrodes without any initial concepts in mind, by verifying the common assumptions used, analyzing the accuracy of the current model predictions, and finally studying the state of the investigations on relevant neglected phenomena. In this section, the particular conditions of the case studied and main limitations are recalled, followed by a summary of the conclusions reached, and, finally, recommendations for future investigations and experiments are given.

The study presented here, even if more general results are derived, is mainly limited to the case of an electrode formed by a metal inlaid disk, embedded in a comparatively large insulating solid planar surface. A large overvoltage with respect to the standard potentials of the mercury redox couples is assumed, as is a relatively high mercury ion bulk concentration. Furthermore, an excess electrolyte in the solution is considered. No forced flow is applied and natural convection is neglected, as are mutual diffusion and alloy formation between the electrode metal and the mercury.

For these conditions, a time-scale analysis is performed. The migration of mercury ions is found to be negligible, and the reduction reaction is found to achieve a quasi-equilibrium at the time scale of the mass transport, which is driven by diffusion. The amalgam is also found to achieve a quasi-equilibrium shape on the diffusional time scale, and thus the amalgam electrodepositon is considered to be a diffusion controlled process. Furthermore, the growth of the amalgam is shown to be sufficiently slow that the diffusion problem can be considered a quasi-steady-state problem.

Based on the time scale analysis, and incorporating a number of models from the literature, theoretical electrodeposition models are developed and analyzed through numerical comparison with current and charge experimental plating curves. The modeling of the current by a steady-state expression increasing through the interface area is found to be satisfactory for long-term experiments, but significantly improved during the early times by the addition of a transient term. This formulation seems able to accurately predict the volume deposition for small microelectrodes (radius $a \leq 2.5\ \mu\mathrm{m}$), but it fails to reliably describe the current evolution for larger electrodes.

After consideration of the electrodeposition models, and due to direct observations available in the literature, the nucleation of multiple droplets and subsequent growth prior to coalescence is proposed as the mechanism responsible for the discrepancy between the models and experiment, and for much of the experimental variability. An investigations of the nucleation process lead us to conclude that it is spontaneous, and allow us to estimate the density of nuclei formed. The coalescence is studied based on the DLVO theory of charged surface interaction, which concentrates on two opposite forces, the Van der Waals attraction and the electrostatic repulsion. The major success of this formulation, incorporated into a statement of mechanical equilibrium, is the prediction of the existence of a critical minimum droplet size for coalescence.

Our study has indicated the possibility of many fruitful areas for further investigations. Our recommendations for future work, based on the most important or interesting remaining issues are listed below.

1 - Development of a better model describing the multiple nucleation process quantitatively based on generally available parameters.

2 - Development of a model able to quantitatively predict the electrode current during the multiple nucleation and growth process.

3 - Further development of the droplet interaction theory. This area is fairly undeveloped and of general interest. Some first steps would be extension of the current formulation to the case of larger applied potentials. The next step should be an incorporation of the effect of the conducting surface, and of the effect of the droplet deformation due to multiple droplet interactions.

4 - Study of processes and the phenomena governing the motion of the droplet contact line during droplet growth. These can include mutual diffusion, molecular long-range

forces and alloy formation. Also needed is an evaluation of the relationship between contact angles and droplet interactions.

5 - Investigation on natural convection phenomena that could occur during electrodeposition experiments and their quantitative influence. In particular, the evolution of gas bubbles is suspected as a potential contributor to experimental variability.

6 - Finally, we outline some experiments that could validate some of our conclusions.

a) Plating experiments with electrode radius $a \geq 12.5\ \mu\text{m}$, with a high sampling rate (greater than 1 kHz), and with measurement beginning before the potential step, should verify the presence and magnitude of the current peak predicted by the nucleation current models. Alternatively, plating experiments with smaller sampling rates could be in conjunction with lower mercury ion concentrations.

b) Plating experiments with electrode radius $a \geq 12.5\ \mu\text{m}$ at a potential close to the electro-capillary maximum, and also with a large electrolyte concentration (1M for example), should verify the spontaneous coalescence predicted in these cases by the DLVO theory.

APPENDIX

SPHERE-CAP GEOMETRY

The following geometric relationships are useful when performing calculations involving segments of spheres (or sphere-caps). The geometric parameters are defined graphically in Figure A-1 [20].

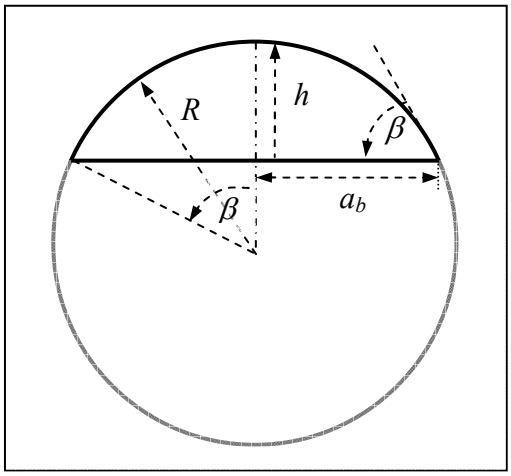

Figure A-1. Sphere-cap geometry.

- Basic relations: $h = R(1-\cos\beta)$

$$a_b = R\sin\beta$$

$$(R-h)^2 + a_b^2 = R^2$$

Surface : $S = 2\pi Rh$

Volume : $V = \frac{1}{3}\pi h^2(3R-h)$

- when the sphere-cap is defined by V and a_b:

$$h = -\frac{a_b^2 \pi}{M} + \frac{M}{\pi} \qquad \text{with} \qquad M = \left(\pi^2 (3V + \sqrt{a_b^6 \pi^2 + 9V^2}) \right)^{1/3}$$

$$R = \frac{a_b^2 + h^2}{2h} \quad \text{and} \quad \beta = \cos^{-1}\left(\frac{R-h}{R}\right)$$

- when the sphere-cap is defined by V and β:

$$R = \left(\frac{3V}{\pi (1-\cos\beta)^2 (2+\cos\beta)} \right)^{1/3}, \qquad h = R(1-\cos\beta)$$

$$a_b = \sqrt{h(2R-h)} \qquad \text{and} \qquad \beta = \cos^{-1}\left(\frac{R-h}{R}\right)$$

REFERENCES

1. J. Kwak and A.J. Bard, *Anal. Chem.*, 1989(61): p. 1221.

2. Y. Selzer and D. Mandler, *Anal. Chem.*, 2000(72): p. 2383.

3. A.J. Bard, F.-R.F. Fan, J. Kwak, and O. Lev, *Anal. Chem.*, 1989(61): p. 132-138.

4. C.G. Zoski, A.M. Bond, E.T. Allinson, and K.B. Oldham, *Anal. Chem.*, 1990(62): p. 37.

5. D. Rudolph, S. Neuhuber, C. Kranz, M. Taillefert, and B. Mizaikoff, *Analyst*, 2004(129): p. 443-448.

6. J.V. Macpherson, P.R. Unwin, A.C. Hillier, and A.J. Bard, *J. Am. Chem. Soc.*, 1996(118): p. 6445-6452.

7. L.P. Bauermann, W. Schuhmann, and A. Schulte, *Phys. Chem. Chem. Phys.*, 2004. **6**(15): p. 4003-4008.

8. Mauzeroll, Hueske, and Bard, *Anal. Chem.*, 2003(75): p. 3880-3889.

9. Z.K. Z. Stojek, *J. Electroanal. Chem.*, 1975. **60**(3): p. 349.

10. M.Z. Hassan, D.F. Tereke, and S. Bruckens, *J. Electroanal. Chem.*, 1973(42): p. 161.

11. O. Mikkelsen and K.H. Schroder, *Electroanalysis*, 2003. **15**(8): p. 679.

12.Bard and Faulkner.
Electrochemical methods: Fundamentals and Applications: Wiley, 2nd edition.

13. Colyer, Luscombe, and Oldham, *J. Electroanal. Chem.*, 1990(283): p. 379-387.

14. Myland and Oldham, *J. Electroanal. Chem.*, 1990(288): p. 1-14.

15.E. Budevski, G. Staikov, and W.J. Lorenz.
Electrochemical Phase Formation and Growth: VCH.

16. IUPAC, *Pure & Appl. Chem.*, 1993. **65**(12): p. 2613.

17. D.C. Grahame, *Chem. Rev.*, 1947(41): p. 441.

18. A.-M. Cazabat, *Contemp. Phys.*, 1987(28): p. 347.

19. C.L. Colyer, K.B. Oldham, and S. Fletcher, *J. Electroanal. Chem.*, 1990(290): p. 33.

20. J.L. Amphlett and G. Denuault, *J. Phys. Chem.*, 1998. **102**: p. 9946.

21. D. Rudolph, K. Kranz, and B. Mizaikoff, *Unpublished data*, 2005.

22. Y. Saito, *Rev. Polarogr. (Jpn.)*, 1968(15): p. 177.

23. K.B. Oldham, *J. Electroanal. Chem.*, 1991. **297**: p. 317.

24. P.J. Mahon and K.B. Oldham, *Electrochimica Acta*, 2004(49): p. 5041.

25. L. Rajendran, *Electrochemistry Communications*, 2000(2): p. 531.

26. D. Shoup and A. Szabo, *J. Electroanal. Chem.*, 1982(140): p. 237.

27. K. Aoki and J. Osteryoung, *J. Electroanal. Chem.*, 1981(122): p. 19.

28. C.G. Phillips, *J. Electroanal. Chem.*, 1992(333): p. 11.

29. S. Toshev and I. Markov, *Ber. Bunsenges. Phys. Chem.*, 1969(73): p. 184.

30. A. Milchev and S. Stoyanov, *J. Electroanal. Chem.*, 1976(72): p. 33.

31. M.E. Hyde and R.G. Compton, *J. Electroanal. Chem.*, 2003(549): p. 1.

32. B. Scharifker and G. Hills, *Electrochimica Acta*, 1983. **28**(7): p. 879.

33. M. Avrami, *J. Chem. Phys.*, 1940(8): p. 212.

34. J. Li, E. Herrero, and H.D. Abruna, *Colloids and Surfaces*, 1998. **A**(134): p. 113.

35. A.I. Danilov, E.B. Molodkina, Y.M. Polukarov, and J.M. Feliu, *Russ. J. Electrochem.*, 2002. **38**(7): p. 254.

36.J. Israelachvili, *Intermolecular and surface forces, 2nd edition*. 1985.

37. N.V. Chuarev, *Advances in Colloid and Interface Science*, 1999(83): p. 19.

38. B.V. Derjaguin and L. Landau, *Acta Physico-chemica, URSS*, 1941(14): p. 633.

39. E.J.W. Verwey and J.T.G. Overbeek, 1948.

40. T. Yamasaki, U. Shinnosuke, and J. Shimoiizaka, *J. Phys. Chem.*, 1967. **71**(10): p. 3195.

41. A. Watanabe and R. Gotoh, *Colloid Polymer Science*, 1963. **191**: p. 36.

42. M.K. Chaudhury, *Journal of Colloid and Interface Science*, 1987. **119**(1): p. 174.

43. G.P. Neitzel and D. Dell'Aversana, *Annu. Rev. Fluid. Mech.*, 2002. **34**: p. 267.